Zymoseptoria tritici proteins structurally related to UmV-KP4 and UmV-KP6 are toxic to fungi, and define novel structural families of fungal effectors

Karine de Guillen[1], Léa Mammri[1], Jérôme Gracy[1], André Padilla[1], Philippe Barthe[1], François Hoh[1], Mounia Lahfa[1], Justine Rouffet[2], Yohann Petit-Houdenot [2], Thomas Kroj[3], Marc-Henri Lebrun[2]

[1] Centre de Biologie Structurale, Université de Montpellier, INSERM U1054, CNRS UMR 5048, 34090 Montpellier, France.

[2] Université Paris-Saclay, INRAE, UR BIOGER, Palaiseau, France

[3] PHIM Plant Health Institute, University of Montpellier, INRAE, CIRAD, Institut Agro, IRD, 34060 Montpellier, France.

Corresponding Author:
Karine de Guillen
karine.deguillen@cbs.cnrs.fr
tel 33 467417708

Abstract

Fungal effectors play crucial roles in plant infection. Despite low sequence identity, their classification into families is feasible using structural homology. In this study, we have elucidated the structures of the two effectors Mycgr3-91409 and Zt-NIP1 from the wheat fungal pathogen *Zymoseptoria tritici* using X-ray crystallography and NMR. These proteins shared structural homology with, respectively, KP6α and KP4 killer toxins, encoded by UmV dsRNA viruses infecting the corn fungal pathogen *Ustilago maydis*. Consequently, Zt-Mycgr3-91409 and Zt-NIP1 were renamed Zt-KP6-1 and Zt-KP4-1. Orthologs and paralogs of Zt-KP6-1 and Zt-KP4-1 were identified in *Zymoseptoria* species, but not in other fungi, with the exception of ECP2 effectors related to Zt-KP4-1. A novel pipeline relying on Foldseek and cysteine-pattern constrained HMM searches identified a large number of proteins structurally related to Zt-KP6-1 and Zt-KP4-1 in fungi, and to Zt-KP4-1 in plants. These proteins were classified into distinct structural super families (4 KP4 and 3 KP6) including effectors not known as structurally related to KP4 (ECP2) or KP6 (BAS4). The biological activities of Zt-KP6-1 and Zt-KP4-1 were assessed on plants and fungi. They did not induce symptoms on wheat leaves. However, they inhibited the growth of *Botrytis cinerea* and *Z. tritici*, demonstrating their toxicity to fungi. These results highlight the importance of structure determination of effectors for their classification and the prediction of their function.

INTRODUCTION

Fungal plant pathogens express secreted proteins without enzymatic functions during host plant infection called effectors (Lo Presti *et al.*, 2015; Li *et al.*, 2024). Most fungal effectors display no or very limited sequence similarities (Outram *et al.*, 2022; Lazar *et al.*, 2022). However, comparison of their three-dimensional structures allowed their classification into families of structurally related proteins (Outram *et al.*, 2022). This strategy was successful in identifying a large number of Magnaporthe AVRs and ToxB-like (MAX) effectors from the fungal rice pathogen *Pyricularia oryzae* sharing the same conserved fold (de Guillen *et al.*, 2015; Le Naour—Vernet *et al.*, 2023; Lahfa *et al.*, 2024). The RNase-like proteins associated with haustoria (RALPH) effectors of the cereal powdery mildew fungus *Blumeria graminis* were also grouped into a family of structurally related proteins using modeling and experimental structure determination (Spanu, 2017; Pennington *et al.*, 2019; Bauer *et al.*, 2021; Cao *et al.*, 2023). Additional families of structurally related fungal effectors were identified using X-ray diffraction (XRD) and modeling in *Leptosphaeria maculans* (Blondeau *et al.*, 2015; Lazar *et al.*, 2020; Talbi *et al.*, 2023; Loubet *et al.*, 2024), *Fusarium oxysporum* (Teulet *et al.*, 2023; Yu *et al.*, 2023), and *Venturia inaequalis* (Rocafort *et al.*, 2022). Recently, the systematic prediction of structures of fungal secreted proteins with different programs including AlphaFold2 (AF2) (Jumper *et al.*, 2021), revealed novel families of structurally related fungal effectors (Seong & Krasileva, 2023; Derbyshire & Raffaele, 2023).

To identify novel families of fungal effectors, we elucidated the three-dimensional structures of the secreted proteins Zt-Mycgr3-91409 and Zt-NIP1 from the wheat fungal pathogen *Zymoseptoria tritici* by X-ray diffraction (XRD) and nuclear magnetic resonance (NMR). Zt-Mycgr3-91409 is an effector upregulated during infection of wheat leaves (Rudd *et al.*, 2015) suggested to be a MAX effector (de Guillen *et al.*, 2015). Zt-NIP1 is expressed during infection of wheat (Rudd *et al.*, 2015; Kilaru *et al.*, 2022) and induces mild chlorotic/necrotic lesions on leaves (Ben M'Barek *et al.*, 2015). Unexpectedly, the structures of Zt-Mycgr3-91409 and Zt-NIP1 shared structural similarities with UmV-KP6α and UmV-KP4 killer toxins encoded by dsRNA viruses infecting the corn fungal pathogen *Ustilago maydis*. UmV-KP6α and UmV-KP4 kill susceptible *U. maydis* strains, while UmV infected strains are resistant to the killer toxin they produce (Finkler *et al.*, 1992; Allen *et al.*, 2013b). Consequently, we renamed Zt-

Mycgr3-91409 to Zt-KP6-1 and Zt-NIP1 to Zt-KP4-1. Proteins structurally related to Zt-KP6-1 or Zt-KP4-1 were widely distributed across fungi and they were classified in families of related structures. Bioassays revealed that Zt-KP6-1 and Zt-KP4-1 were not toxic to wheat leaves, but inhibited fungal growth.

82 **RESULTS**

83

84 **Zt-Mycgr3-91409-2 is a structural homolog of UmV-KP6 killer toxin**

85

86 Zt-Mycgr3-91409 gene model was curated according to transcript evidence (Lapalu *et*
87 *al.*, 2023) (Sup Figure 1A). Zt-Mycgr3-91409-2 (SMR48303, A0A2H1G421) was
88 expressed in *Escherichia coli* and purified by size exclusion chromatography (SEC)
89 (Sup File S1, Sup Figure 2). High-resolution diffracting crystals were obtained after
90 crystallization screens and optimization of Li_2SO_4 concentration and pH then soaked
91 in tantalum. Analyses of XRD data at 1.36 Å resolution showed that crystals belonged
92 to the $P2_12_12_1$ space group with two copies of the protein per asymmetric unit. The
93 structure of Zt-Mycgr3-91409-2 solved by single-wavelength anomalous diffraction
94 (SAD) revealed that the protein had a typical α/β sandwich structure (Figure 1, Sup
95 Table 1). This fold has two α-helices and four β-strands arranged in an antiparallel β-
96 sheet with one hairpin connection formed by the short strands β2-β3 and two βαβ
97 connections, which placed the α-helices in an antiparallel manner on one side of the
98 β-sheet.

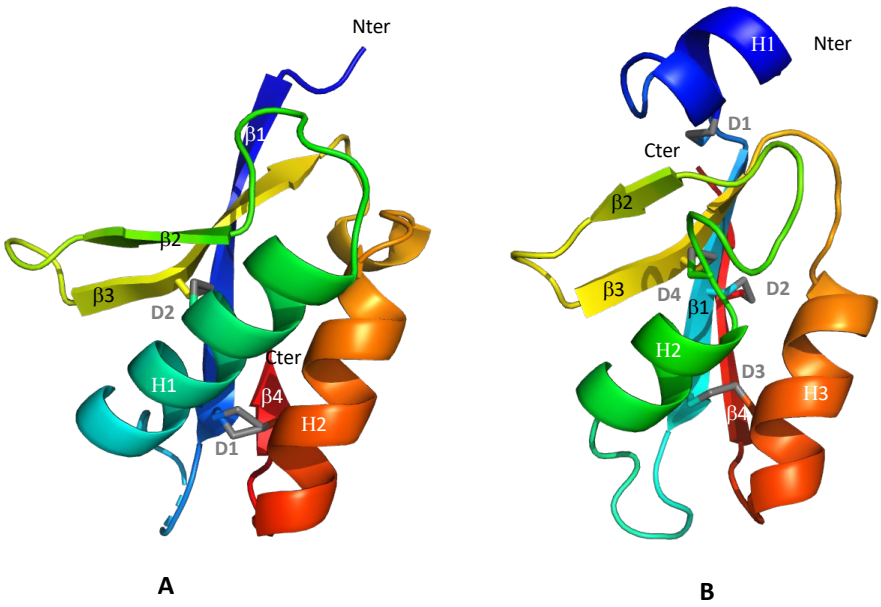

Figure 1

99

100 Figure 1. *Crystal structures of (A) Zt-KP6-1 (6QPK chain A) and (B) UmV-KP6α (4GVB*
101 *chain A).*
102 *(A) Zt-Mycgr3-91409-2 was renamed to Zt-KP6-1 according to its structural similarity*
103 *to UmV-KP6α (see text). Structures were colored in rainbow colors from blue (N*
104 *terminus) to red (C terminus). For Zt-KP6-1, the loop connecting β1 (in blue) to H1 (in*
105 *cyan) was not observed in the density map and is shown as a blue dashed line.*
106 *Disulphide bonds are shown in grey and labelled Dx. For the D1 (C26-C86) bond in Zt-*
107 *KP6-1, both conformations are shown.*
108
109 The α-helix H2 was preceded by a 3^{10} helix formed by residues 77 to 89 (numbering
110 according to the mature protein). Both α-helices (H1 and H2) were tightly packed
111 against the β-sheet, with one disulphide bond formed between cysteine residues in β1
112 (Cys26) and H2 (Cys86) and another disulphide bond formed between cysteine
113 residues in H1 (Cys43) and β3 (Cys65), making the fold very compact. Alternative
114 conformations were observed for Cys26 involving the disulphide bond with Cys86. The
115 interface area between the two monomers observed in the crystal, determined by
116 PDBePISA, was estimated to be 435.8$Å^2$. The Complexation Significance Score (CSS)
117 was 0, indicating that the dimer has no biological relevance and resulted from crystal
118 packing. NMR studies of the protein labelled with ^{15}N revealed a high similarity to the
119 crystal structure, with an r.m.s.d. of 0.7 ± 0.6 Å on structured parts. However, the
120 protein was not dimeric in solution, as shown by the narrowness of the ^{1}H-^{15}N HSQC
121 spectrum peaks (Sup Figure 3 and Sup Table 2), and the single elution profile at 95
122 min observed in SEC corresponding to a retention time of a 9 kDa globular protein
123 (Sup Figure 2).
124
125 A DALI analysis (Holm, 2020) revealed structural similarity between Zt-Mycgr3-91409-
126 2 and UmV-KP6α (PDB 4GVB, Figure 1). UmV-KP6α is encoded by a dsRNA virus
127 infecting *U. maydis,* a fungal pathogen causing corn smut disease (Allen *et al.*, 2013b).
128 UmV-KP6α is produced together with UmV-KP6β by cleavage of the UmV-KP6 pre-
129 protein encoded by the virus. UmV-KP6α has eight cysteine residues, while UmV-
130 KP6β has six cysteines, all involved in intramolecular disulphide bonds. Both UmV-
131 KP6α and UmV-KP6β have a highly similar fold (Li *et al.*, 1999; Allen *et al.*, 2013b). Zt-
132 KP6-1 structure was more similar to UmV-KP6α (Z-score of 6.7 and r.m.s.d of 2.5 Å
133 for 63 aligned residues). However, Zt-KP6-1 did not have the N-terminal hydrophobic

α-helix extension present in UmV-KP6α. The KP6 protein fold shared between UmV-KP6α, UmV-KP6β and Zt-KP6-1, is defined by two α-helices (H1 and H2) positioned on one side of a 4-stranded β-sheet, with a β4-β1-H1-β3-H2-β2topology (Sup Figure 4). All three proteins have two right handed β-α-β split crossovers, which distinguish the KP6 protein fold from toxins of similar size (Allen *et al.*, 2013a). The KP6 protein fold also shared two disulphide bonds that link the antiparallel α-helices to the central β-sheet of the protein (Sup. Fig. 4). According to these structural similarities, Zt-Mycgr3-91409-2 was renamed Zt-KP6-1.

Zt-NIP1 is a structural homolog of *UmV*-KP4 killer toxin

Zt-NIP1 was identified as a wheat necrosis-inducing protein produced by IPO323 *Z. tritici* isolate during wheat leaf infection (Ben M'Barek *et al.*, 2015). However, the CDS at the *Zt-NIP1* locus in IPO323 genome (*Zt-Mycgr3-106176*) encoded a protein with a sequence unrelated to NIP1. A new CDS, almost identical to NIP1 (99% identity), was predicted in agreement with transcript evidence (Lapalu *et al.*, 2023) (Sup Figure 1B). Zt-NIP1 (SMR6055, A0A2H1H404) was expressed in *Escherichia coli* and purified by SEC (Sup File S1). SEC revealed an equilibrium between Zt-NIP1 monomers and dimers in solution (Sup Figure 5). High-resolution diffracting Zt-NIP1 crystals were in the *H3* space group with 8 copies of the protein per asymmetric unit (Sup Table 1). The Zt-NIP1 structure was solved by molecular replacement using an AF2 model (Figure 2). The protein has a typical α/β sandwich structure with a single split βαβ motif and two disulphide bonds. A main antiparallel 5 stranded β-sheet is formed by β1-β3-β4-β6-β7, with a second small antiparallel 2 stranded β-sheet comprising β2 and β5 (with 4 residues each). Two α-helices (H1 and H2) close the structure. The fold is held together by two disulphide bonds formed between cysteine residues in β2 (Cys39) and β7 (Cys142), and H1 (Cys60) and β4 (Cys89). Chains E-H, G-B, F-C, and D-A formed dimers, through the main 5 stranded β-sheet, in the crystal structure, with an average interface area of 852.2 $Å^2$ determined by PDBePISA. These dimers exhibited a CSS score of 1.0, which indicates the biological significance of such a dimer (Sup Figure 6).

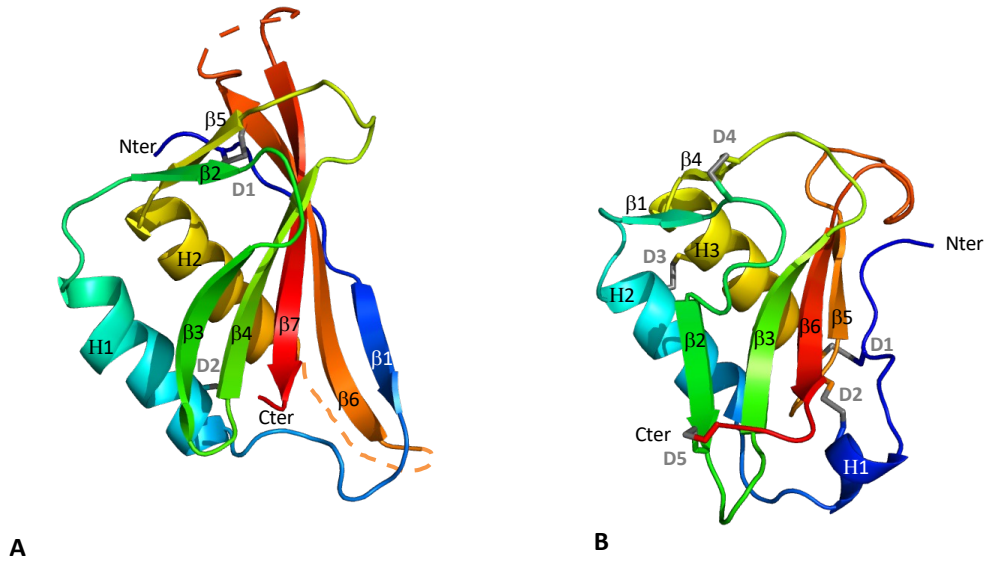

Figure 2

Figure 2. *Crystal structures of (A) Zt-KP4-1 (8ACX chain A) and (B) UmV-KP4 (1KPT chain A).*
(A) Zt-NIP1 was renamed to Zt-KP4-1 according to its structural similarity to UmV-KP4 using DALI (see main text). Structures were colored in rainbow colors from blue (N terminus) to red (C terminus). For Zt-KP4-1 the loops connecting β6 to β7 and β6 to H1 were not observed in the density map and were shown as dashed lines. Disulphide bonds are shown in grey and labelled Dx.

A DALI analysis (Holm, 2020), revealed structural similarity between Zt-NIP1 and UmV-KP4 (PDB 1KPT, Figure 2). UmV-KP4 is encoded by a dsRNA virus infecting *U. maydis* (Allen *et al.*, 2013b). The two proteins superposed with a Z-score of 7.3 and a r.m.s.d value of 2.4 Å (82 residues aligned). UmV-KP4 (Koltin, 1988; Gu *et al.*, 1995) belongs to the α/β sandwich family of proteins and is composed of seven β strands and three α-helices. Similar to Zt-NIP1, UmV-KP4 has two helices (H2 and H3) in a left-handed βαβ crossover conformation, which is a rare structural feature (Sup Figure 7) (Allen *et al.*, 2013a). The main difference between the two proteins is the presence of a β-strand (β1) at the N-terminus for Zt-NIP1 instead of a short α-helix (H1) for UmV-

184 KP4. The two proteins also differ in the number and location of disulphide bonds. While
185 Zt-NIP1 has two disulphide bonds (as described above), UmV-KP4 has five. Based on
186 the structural similarity of these proteins, Zt-NIP1 was renamed to Zt-KP4-1.
187
188 **Zt-KP4 and Zt-KP6 are toxic to fungi**
189
190 Zt-KP4-1 and Zt-KP6-1 (each at a concentration of 2 μM) were infiltrated into leaves of
191 the wheat cultivar Taichung 29 which is susceptible to *Z. tritici*. Neither of the two
192 proteins induced visible signs of toxicity such as leaf chlorosis or necrosis. In the same
193 experiment, infiltration of the necrotrophic effector ToxA from *P. nodorum* (Tan *et al.*,
194 2012) into Taichung 29 wheat leaves induced typical necrotic lesions at concentrations
195 ranging from 0.2 to 2 μM. To test if Zt-KP4-1 and Zt-KP6-1 are toxic to fungi, growth
196 assays were performed in liquid potato dextrose growth medium complemented with
197 recombinant Zt-KP4-1 or Zt-KP6-1 at different concentrations (0.55 to 5.5 μM). The *Z.*
198 *tritici* IPO323 isolate, which expresses both Zt-KP4-1 and Zt-KP6-1, and the
199 necrotrophic plant pathogen *Botrytis cinerea* were used for these bioassays. Zt-KP4-1
200 strongly inhibited the growth of both fungi at 5.5 μM (91-95 % inhibition, Table 1).
201 However, at 1.65 μM, only *Z. tritici* growth was inhibited (48 % inhibition, Table 1). Zt-
202 KP6-1 was as toxic as Zt-KP4-1 on *B. cinerea* (94 % inhibition at 5.5 μM, Table 1).
203 However, it only weakly inhibited the growth of *Z. tritici* (24 % inhibition at 5.5 μM, Table
204 1). These results demonstrate that Zt-KP4-1 and Zt-KP6-1 are not toxic to wheat leaves
205 but are toxic to fungi at concentrations below those measured for fungal toxic proteins
206 (20 μM) (Kettles *et al.*, 2018; Lima *et al.*, 2022). While Zt-KP4-1 displayed the same
207 toxicity to *Z. tritici* and *B. cinerea,* Zt-KP6-1 displayed some quantitative selectivity, as
208 *Z. tritici* was 4-fold less sensitive than *B. cinerea*.
209

		% inhibition	
		Botrytis cinerea	***Zymoseptoria tritici***
Protein concentration (µM)			
TOX A	5.50	25 ± 1.4	0
	1.65	0	0
	0.55	0	0
Zt-KP4-1	5.50	91 ± 3.2	95 ± 1.4
	1.65	0	48 ± 2.2
	0.55	0	25 ± 1.4
Zt-KP6-1	5.50	94 ± 2.0	24 ± 1.2
	1.65	0	0
	0.55	0	0

210

211 Table 1. *Toxicity of Zt-KP4-1 and Zt-KP6-1 to fungi*

212 *The percentages of* B. cinerea *and* Z. tritici *growth inhibition were calculated for*
213 *different concentrations of ToxA, Zt-KP4-1and Zt-KP6-1. Values are the mean ±*
214 *Standard Error of the Mean (SEM) from three experiments.*

215

216 **Identification of Zt-KP6-1 homologs in *Zymoseptoria***

217

218 Proteins with sequences highly similar to Zt-KP6-1 were identified in other strains of *Z.*
219 *tritici* (Badet *et al.*, 2020) and *Z. pseudotritici* (Zp-KP6-1, 92% identity, Figure 3), but
220 not in other *Zymoseptoria* species. Another protein family with a relatively low
221 sequence identity to Zt-KP6-1 (28-30%) was identified in *Z. tritici* (Zt-KP6-2) and other
222 *Zymoseptoria* species (KP6-2 from *Z. brevis, Z. arbibiliaie* and *Z. pseudotritici*, Figure
223 3). The structure of Zt-KP6-2 protein predicted by AF2 was similar to Zt-KP6-1 (Z-score
224 of 12.1; r.m.s.d of 1.9 Å for 73 aligned residues, Sup Figure 8). This comparison
225 highlighted an 11 amino acid C-terminal sequence with two cysteine residues
226 conserved in all KP6-2 proteins, but absent from KP6-1 proteins. Proteins similar to Zt-
227 KP6-1 and Zt-KP6-2 were not identified in other fungi. The phylogenetic analysis of
228 KP6-1 and KP6-2 proteins from different *Zymoseptoria* species highlighted two clades
229 gathering orthologous proteins from *Zymoseptoria* (Figure 3). This topology suggested
230 that KP6-1 and KP6-2 are paralogs originating from the duplication of an ancestral
231 gene before the divergence of *Zymoseptoria* species.

232

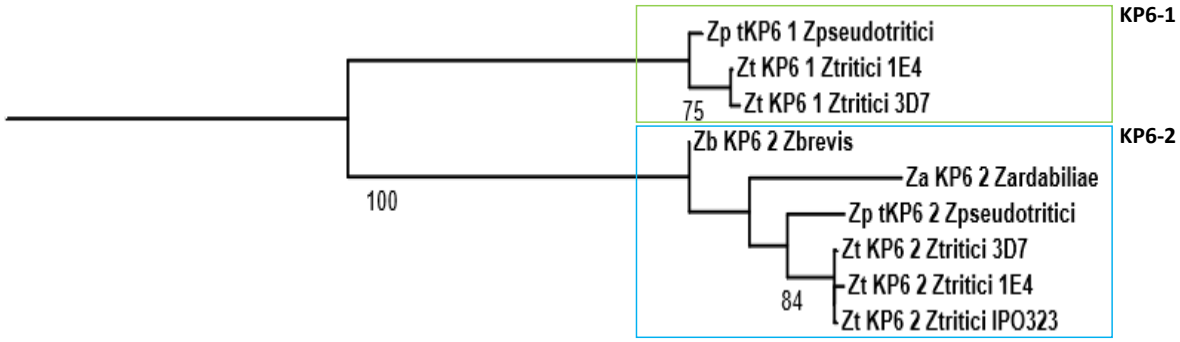

Figure 3. Phylogenetic tree of *Zymoseptoria* KP6-1 and KP6-2

MAFFT alignment, BMGE cleaning, PhyML Phylogenetic tree using NGPhylogeny.fr. (Lemoine *et al.*, 2019) Bootstrap values > 70% are indicated under each branch after the supported node. Midpoint tree rooting. Zt-KP6-1_Ztritici_3D7: Uniprot A0A1X7RM13 (identical to Zt-KP6-1_IPO323); Zt-KP6-1_Ztritici_1E4: Uniprot A0A2H1G421, PDB 6QKP; Zp-KP6-1_Zpseudotritici: JGI Zymps1_802032; Zt-KP6-2_Ztritici_1E4: Uniprot A0A2H1H0K4; Zt-KP6-2_Ztritici_IPO323: Uniprot F9XLY9; Zt-KP6-2_Ztritici_3D7: Uniprot A0A1X7S5L2; Zb-KP6-2_Zbrevis: Uniprot A0A0F4GMG5; Za-KP6-2_Zardabiliae: JGI Za_774343 ; Zp-KP6-2_Zpseudotritici: JGI Zymps1_805921.

Using a pipeline based on FoldSeek and Hmmer (Sup Figure 10), we searched for proteins structurally related to Zt-KP6-1 and Zt-KP6-2 in *Zymoseptoria*. The structures of the retrieved proteins were predicted using AF2 and visually inspected for structural overlaps with Zt-KP6-1. Three proteins were structurally related to Zt-KP6-1: Zt-KP6-4, Zt-KP6-5 and Zb-KP6-6. However, Zt-KP6-3 did not share sufficient structural similarity to KP6-1 (DALI score of 0) to be selected and it was excluded from further analyses.

Identification of Zt-KP4-1 homologs in *Zymoseptoria*

Proteins with sequences highly similar to Zt-KP4-1 were identified in other strains of *Z. tritici* (Badet *et al.*, 2020) (Figure 4), but not in other *Zymoseptoria* species. Two other protein families with a relatively low sequence identity to Zt-KP4-1 (33-35%) were identified in *Z. tritici* (Zt-KP4-2, 35% identity; Zt-KP4-3, 33% identity) and *Z. brevis* (Zb-KP4-2; Zb-KP4-3). The structures of *Zymoseptoria* KP4-2 and KP4-3 proteins

predicted with AF2 were similar to Zt-KP4-1 (Sup Figure 9). A phylogenetic analysis of *Zymoseptoria* KP4-1, KP4-2 and KP4-3 was performed using related ECP2 proteins as outgroups (Van den Ackerveken *et al.*, 1993; Chang *et al.*, 2016; Carreón-Anguiano *et al.*, 2023). ECP2 proteins were retrieved as the top hits in BlastP searches of the proteomes of the corresponding fungi using Zt-KP4-1 and Zt-KP4-2 as queries, although with relatively low scores (28-32% identity, e-value 10^{-20}). The *Zymoseptoria* KP4-1, KP4-2 and KP4-3 proteins clustered as three independent clades gathering orthologous proteins from *Zymoseptoria*. These three clades were rooted by ECP2 proteins from other fungi (Figure 4). This topology suggested that KP4-1, KP4-2 and KP4-3 originated from duplications of an ancestral gene, prior to the divergence of *Zymoseptoria* species.

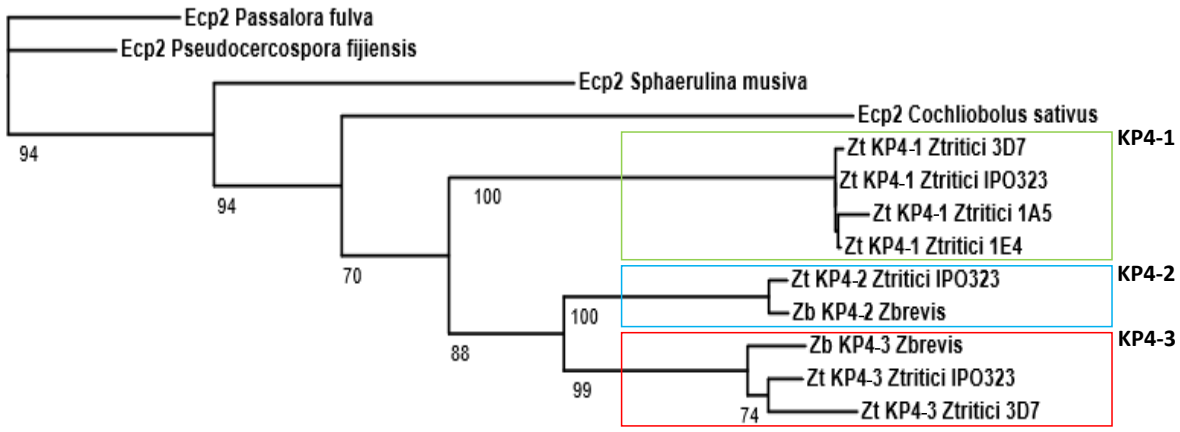

Figure 4: Phylogenetic tree of *Zymoseptoria* KP4-1, KP4-2 and KP4-3

MAFFT alignment, BMGE cleaning, PhyML Phylogenetic tree using NGPhylogeny.fr (Lemoine *et al.*, 2019). Bootstrap values > 70% are indicated under each branch after the supported node. Tree root with Ecp2_Passalora fulva and Ecp2_Pseudocercospora fijiensis as outgroups. Zt-KP4-1_Ztritici_IPO323: re-annotated NIP1/Mycgr3-106176 see Sup. Fig1; Zt-KP4-1_Ztritici_1E4: Uniprot A0A2H1H404; Zt-KP4-1_Ztritici_3D7: Uniprot A0A1X7S6U3; Zt-KP4-1_Ztritici_1A5: Uniprot A0A1Y6M012; Zt-KP4-2_Ztritici_IPO323: Mycgr3-107904, Uniprot F9X223; Zb-KP4-2_Zbrevis: KJY02238, Uniprot A0A0F4GYX0; Zt-KP4-3_Ztritici_IPO323: Mycgr3-111636, Uniprot F9XQ02; Zt-KP4-3_Ztritici_3D7: Uniprot A0A1X7S9R6; Zb-KP4-3_Zbrevis: KJX96086, Uniprot A0A0F4GF74; Ecp2_Passalora fulva: Uniprot

285 Q00365; Ecp2_Pseudocercospora fijiensis: Uniprot M2Z6V3; Ecp2_Sphaerulina
286 musiva: Uniprot N1QK49; Ecp2_Cochliobolus sativus: Uniprot M2TE34
287
288 Using a pipeline based on FoldSeek and Hmmer (Sup Figure 10), we searched for
289 proteins structurally related to Zt-KP4-1, Zt-KP4-2 and Zt-KP4-3 in *Zymoseptoria*.
290 *Zymoseptoria* KP4-1, KP4-2 and KP4-3 have an HCE2 domain (PF14856). This
291 domain was defined using proteins related to the fungal effector ECP2 from *P. fulvum*
292 (Stergiopoulos *et al.*, 2012). Therefore, *Zymoseptoria* proteins with an HCE2 domain
293 were retrieved from Uniprot. The HCE2 domain is a multi-gene superfamily that has
294 been named Hce2 for homologues of the *C. fulvum* effector Ecp2, which is widely
295 distributed in fungi, with a putative function as a necrosis-inducing factor. The
296 structures of these proteins were predicted using AF2 and visually inspected for
297 structural overlaps with Zt-KP4-1. This analysis identified four additional proteins
298 structurally related to Zt-KP4-1: Zt-KP4-5, Zt-KP4-6, Zt-KP4-7 and Zt-KP4-9. Two
299 proteins, Zt-KP4-4 and Zt-KP4-8, were not sufficiently structurally to KP4-1 to be
300 selected, despite the presence of the same number of α–helices and β strands
301 organized in the same order as in Zt-KP4-1. In Zt-KP4-4, the structures of the β2 and
302 β5 strands were not well defined (twisted), and the β2-β3 and β5-β6 interactions were
303 reduced. In Zt-KP4-8, the interactions between the β1 and β4 strands were missing.
304 These two proteins were excluded from further analyses.
305
306 ***Zymoseptoria KP4* and *KP6* are expressed during infection**
307
308 Available IPO323 RNA-Seq data (Rudd *et al.*, 2015) were used to retrieve the
309 expression patterns of Zt-KP4 and Zt-KP6 (Sup Fig. 11). *Zt-KP4-5, Zt-KP4-6* and *Zt-*
310 *KP4-7* were expressed at low levels (1/10th of beta-tubulin *TUB1*) in all conditions, while
311 *Zt-KP4-9* was not expressed. *Zt-KP4-1* was the most highly expressed *Zt-KP4* gene
312 during infection of wheat leaves (25 x *TUB1*), with maximum expression at 9 dpi. It was
313 also expressed during *in vitro* growth, although to a lesser extent. *Zt-KP4-3* was
314 expressed during infection at 9 and 14 dpi, and during *in vitro* growth. *Zt-KP4-2* was
315 constitutively expressed at a level similar to *TUB1*. *Zt-KP6-1*, *Zt-KP6-2*, *Zt-KP6-4* and
316 *Zt-KP6-6* displayed a similar expression pattern with maximum expression during
317 infection at 9 dpi and highly reduced expression during *in vitro* growth (100 times less
318 than during infection). This survey showed that most *Zymoseptoria KP4* and *KP6* were

319 over-expressed during the switch from the asymptomatic phase to the necrotrophic
320 phase of infection (9-14 dpi). This switch is associated with the massive colonization
321 of the apoplast of the infected wheat leaf by infectious hyphae of *Z. tritici*, and their
322 invasion of sub-stomatal cavities where they differentiate into pycnidia (Battache *et al.*,
323 2022).
324
325 **Proteins with Zt-KP6-1 structural folds are widespread in fungi**
326
327 Structure modelling of Ecp28-1, Ecp28-2 and Ecp28-3 effectors from the tomato
328 pathogen *Passalora fulvum* (Mesarich *et al.*, 2018) suggested that they have a KP6
329 fold. AF2 structure modelling of these proteins supported this hypothesis (DALI Z score
330 of 7.4). We used our pipeline (Sup Figure 10) to detect fungal proteins structurally
331 related to Zt-KP6-1 in 1014 fungal genomes. The KP6 candidates were selected if their
332 AlphaFold models had a TM-score above 0.5 compared to either Zt-KP6-1 or UmV-
333 KP6α using TM-Align (Zhang & Skolnick, 2005). A total of 1506 KP6 candidates were
334 identified and grouped into 81 AFDB50 clusters (kclXX-Y). The representative proteins
335 of these AFDB50 clusters were merged into 46 meta-clusters (kclXX) (Sup Figure 10).
336 The structure of one representative protein from each meta-cluster was visually
337 inspected using PyMOL for the occurrence of a typical KP6 topology. This analysis
338 rejected nine meta-clusters. The remaining meta-clusters consisted of 1148 proteins
339 with a KP6 fold (sup Table 3) including ECP28 (kcl14), Zt-KP6-1 (kcl06), Zt-KP6-2
340 (kcl06), Zt-KP6-4 (kcl02), Zt-KP6-5 (kcl07) and Zt-KP6 (kcl07). Several fungal effectors
341 have recently been described as KP6 proteins: AvrLm10A and AvrLm6 from *L.*
342 *maculans* (Talbi *et al.*, 2023; Loubet *et al.*, 2024), SIX5 from *Fusarium oxysporum*
343 (Talbi *et al.*, 2023), BAS4 from *Pyricularia oryzae* (Khang *et al.*, 2010), and Cb-Nip1
344 from *Cercospora beticola* (Ebert *et al.*, 2021). The systematic analysis of the structures
345 of the effectors of *V. inaequalis* and *L. maculans* also revealed 108 and 13 KP6
346 proteins, respectively (Rocafort *et al.*, 2022; Loubet *et al.*, 2024). Only few of these
347 proteins were identified in our analysis, since most were not in Uniprot. We added
348 these proteins to meta-cluster representatives. A visual inspection of the structural
349 overlaps between these additional proteins and Zt-KP6-1 rejected only Cb-NIP1, since
350 its AF2 model was not sufficiently structured to allow its superposition to Zt-KP6-1.
351
352 The structures of the 36 selected KP6 proteins were compared using a principal

353 component analysis (PCA) with DALI Z-scores (Figure 5). This analysis highlighted
354 three groups of structurally related KP6 proteins. Group-1 included AvrLm6 and
355 AvrLm10A from *L. maculans* and SIX5 from *F. oxysporum,* but not KP6 proteins from
356 *Zymoseptoria.* Group-2 contained Zt-KP6-4, ECP28, BAS4, four cluster
357 representatives (kcl01-C, kcl02-G, kcl04-A, kcl11), and UmV-KP6β. Group-3
358 encompassed Zt-KP6-1, UmV-KP6α, Zt-KP6-2, Zt-KP6-6, and cluster representative
359 kcl02-A.
360

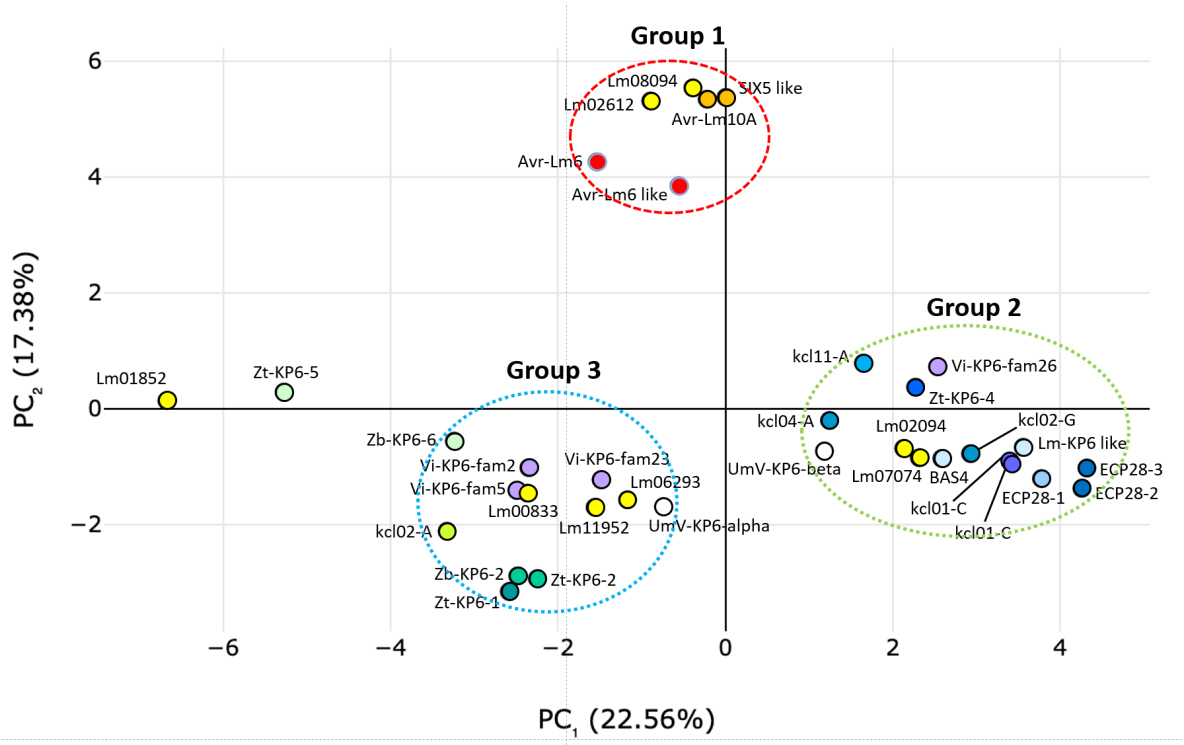

361

362 Figure 5 Classification of fungal KP6 families according to their structures
363 DALI all by all analysis followed by a PCA using a DALI score matrix (Holm, 2020).
364 meta-cluster kclXX, cluster AFDB50 kclXX-Y, (number of proteins in AFDB50 cluster), Uniprot
365 representative (example A0A2H1G421): kcl01-C, (100), A0A4V3HRP1, M1W1H7; kcl01-L,
366 (65), SIX5 = A0A010RIE2, AvrLm10A = E5A720_LEPMJ; kcl02-A, (5), A0A4R8TM13; kcl02-
367 D, (138), Zt-KP6-4 = A0A2H1GZA7; kcl02-G, (321), A0A135SXI2; BAS4 = BAS4_MAGO7,
368 Lm-KP6 = E5A0W1_LEPMJ; kcl04-A, (1), F9FAC2; kcl04-C, (25), AvrLm6 = A0A010QJV2;
369 AvrLm6 = E5R515_LEPMJ; kcl06-A, (6), Zb-KP6-2 = A0A0F4GMG5, Zt-KP6-2 =
370 A0A2H1H0K4; kcl06-B, (3), Zt-KP6-1 = A0A2H1G421/6QKP; kcl07-A, (5), Zt-KP6-5 =
371 A0A2H1FMK1, Zb-KP6-6 = A0A0F4GGQ1; kcl11-A, (6), A0A317AKI4; kcl14-A, (93), ECP28-
372 2 = A0A1P8YXM1, ECP28-3 = A0A1P8YXM5; kcl14-B, (14), ECP28-1 = A0A1P8YXQ5;
373 LmXXXX, *Leptosphaeria* KP6 proteins, (8 proteins, (Loubet *et al.*, 2024)); Vi-KP6-famXX,
374 *Venturia* KP6 proteins, (4 families,(Rocafort *et al.*, 2022)); White circle, UmV-KP6α, 4gvbA,

375 White circle, UmV-KP6β, 4gvbB
376
377 **Proteins with Zt-KP4-1 structural folds are also widely distributed in fungi**
378
379 The HCE2 domain (PF14856) detected in KP4-1, KP4-2 and KP4-3 relies on a pattern
380 of three conserved cysteine residues and a W/F/Y motif (Stergiopoulos *et al.*, 2012).
381 The KP4 domain (PF09044) defined for *F. graminearum* proteins Fg-KP4-1, Fg-KP4-
382 2 and Fg-KP4-3 and UmV-KP4 relies on a pattern involving four conserved cysteine
383 residues, three conserved glycine residues and two W/F/Y motifs (Brown, 2011; Lu &
384 Faris, 2019). We did not detect overlaps in proteins retrieved independently from
385 Uniprot with either the HCE2 or the KP4 domain. Fungal proteins with an HCE2 domain
386 retrieved from Uniprot included Zt-KP4-1, Zt-KP4-2 and Zt-KP4-3. There were no
387 *Zymoseptoria* proteins with a KP4 domain. Additional KP4 proteins were detected
388 using our pipeline (Sup Figure 10) using Zt-KP4-1 and UmV-KP4 as references. A total
389 of 3722 KP4 candidates were identified and grouped into 153 AFDB50 clusters. The
390 representative proteins of these AFDB50 clusters were merged into 59 meta-clusters.
391 The structure of one representative protein from each meta-cluster was visually
392 inspected using PyMOL for the occurrence of a typical KP4 topology. This analysis
393 rejected 31 meta-clusters. The remaining meta-clusters contained 2825 proteins with
394 a KP4 fold (sup Table 4) including ECP2 (kcl01), Zt-KP4-1 (kcl01), Zt-KP4-2 (kcl07),
395 Zt-KP4-3 (kcl07), Zt-KP4-5 (kcl18), Zt-KP4-6 (kcl09), Zt-KP4-7 (kcl09) and Zt-KP4-9
396 (kcl02). We added Fg-KP4-1, Fg-KP4-2 and Fg-KP4-3, which were used to define the
397 KP4 domain, to our analysis (Brown, 2011; Lu & Faris, 2019). These proteins were
398 members of meta-cluster kcl02, but they were not selected as representative of this
399 cluster. Visual inspection of these proteins confirmed their structural similarity to Zt-
400 KP4-1.
401
402 The structures of the 26 selected KP4 proteins were compared using a PCA with DALI
403 Z-scores (Figure 6). This analysis highlighted four groups of structurally related KP4
404 families. Group-1 included Fg-KP4-1, Fg-KP4-2 and Fg-KP4-3, UmV-KP4 and kcl02
405 representative. All these proteins had a KP4 domain. Group-2 contained Zt-KP4-1, Zt-
406 KP4-2 and Zt-KP4-3 and ECP2, as well askcl07, kcl10 and kcl14 representatives. All
407 proteins from Group-2 had an HCE2 domain. Group-3 included the representatives of
408 the clusters kcl08-A and kcl38-A. Proteins from Group-3 did not have known Pfam

domains, except kcl38-A proteins which contained the domain PF15474. Group-4 contained all the other KP4 proteins, including Zt-KP4-5, Zt-KP4-6, Zt-KP4-7 and Zt-KP4-9. Proteins from Group-4 did not have a Pfam domain, except kcl21-A proteins which contained the domain PF21691.

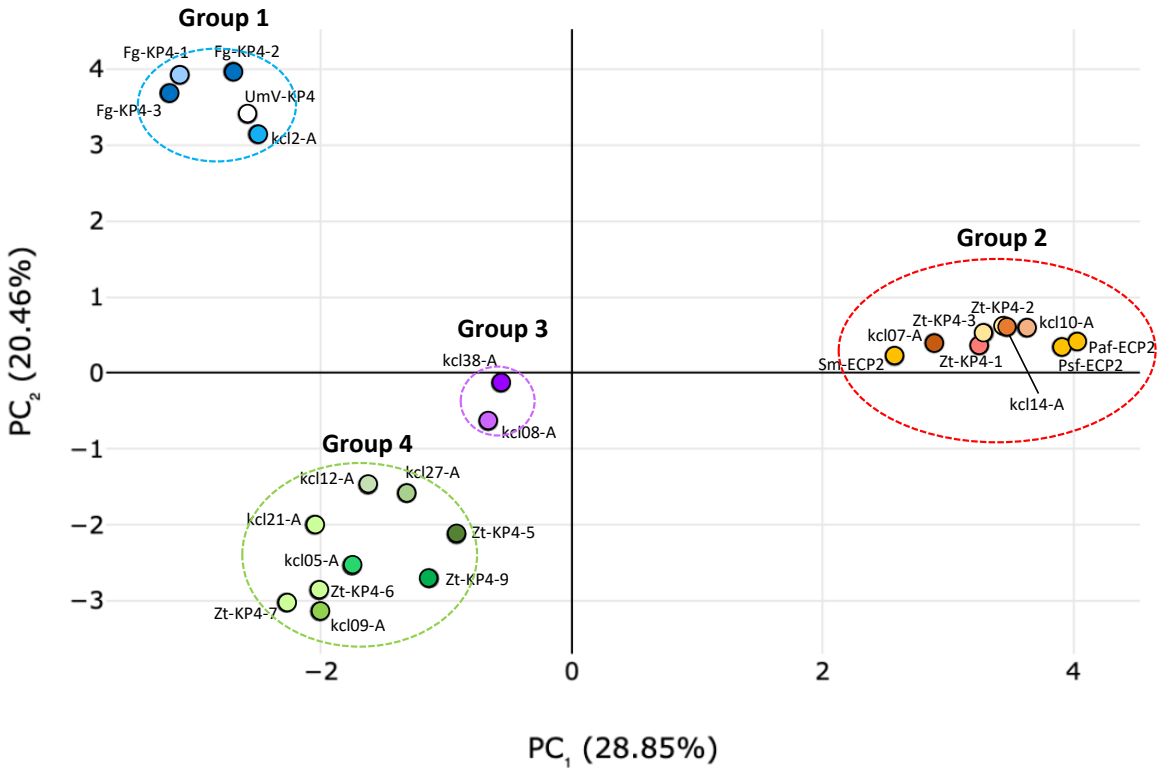

Figure 6 Classification of fungal KP4 families according to their structures

DALI all by all analysis followed by a PCA using a DALI score matrix (Holm, 2020). meta-cluster kclXX, cluster AFDB50 kclXX-Y, (number of proteins in AFDB50 cluster), Uniprot representative (example A0A2H1H404): kcl01-D, (83), Zt-KP4-1 = A0A2H1H404/8ACX; kcl01-Q, (203), Sm-ECP2 = N1QK49, Psf-ECP2 = M2Z6V3, Paf-ECP2 = Q00365; kcl02-A, (15), A0A4U0XEI9; kcl02-E, (256), Fg-KP4-2 = A0A3S7E9S6, Fg-KP4-3 = A0A2H3GQS6; kcl02-I, (125), Fg-KP4-1 = A0A2H3GK41; klc02-0, (324), Zt-KP4-9 = A0A2H1GXX1; kcl05-A, (14), A0A6A6DAE0; kcl07-A, (53), A0A177DVW3; kcl07-C, (35), Zt-KP4-2 = A0A2H1FWY7; Zt-KP4-3 = A0A1Y6M296; kcl08-A, (5), S3D5P; kcl09-A, (14), M3BT27; kcl09-B, (131), Zt-KP4-6 = A0A2H1GNH3, Zt-KP4-7 = A0A2H1GND9; kcl10-A, (16), A0A1L9SH47; kcl12-A, (9), E3L0Y8; kcl14-C, (12), A0A0A1V5R3; kcl18-A, (9), Zt-KP4-5 = A0A2H1GP20; kcl21-A, (13), A0A0J9W663; kcl27-A, (39), A0A4T0WCM2; kcl38-A, (8), A0A017SS08; White circle, UmV-KP4 = kptA

430 **DISCUSSION**

431

432 Comparison of the structures of fungal effectors allowed their classification into families
433 of proteins with related structures (de Guillen *et al.*, 2015; Seong & Krasileva, 2023;
434 Derbyshire & Raffaele, 2023). In this study, the elucidation of the structure of two
435 *Zymoseptoria tritici* effectors (Zt-Mycgr3-91409-2, Zt-NIP1) by X-ray crystallography
436 showed their unexpected structural similarity to the UmV-KP6α and UmV-KP4 killer
437 toxins from the dsRNA virus infecting the fungal pathogen *U. maydis*. Therefore, they
438 were renamed Zt-KP4-1 and Zt-KP6-1. We showed that both effectors were toxic to
439 fungi, but not to wheat leaves. In addition, we found that proteins structurally related to
440 Zt-KP4-1 and Zt-KP6-1 are widespread in fungi, and could be classified into super
441 families of structurally related proteins (4 KP4 and 3 KP6).

442

443 ***UmV*-KP6 and *UmV*-KP4 killer toxins**

444

445 *U. maydis* secretes three killer proteins (UmV-KP1, KP4 and KP6) encoded by double-
446 stranded RNA viruses (UmV) (Tao *et al.*, 1990; Gage *et al.*, 2001; Allen *et al.*, 2013b).
447 They kill susceptible *U. maydis* strains, while UmV-infected strains are resistant to the
448 killer protein they produce (Finkler *et al.*, 1992; Allen *et al.*, 2013b). UmV-KP4 inhibits
449 fungal growth presumably by perturbing cellular calcium homeostasis (Gage *et al.*,
450 2001). UmV-KP4 also inhibited L-type voltage-gated (LVG) Ca^{2+} channels in
451 mammalian cells (Gage *et al.*, 2002). UmV-KP4 inhibited *A. thaliana* root growth, and
452 perturbed Ca^{2+} gradients of root hair cells (Allen *et al.*, 2008). The *P. patrens* moss
453 KP4 protein also modified Ca^{2+} gradients of moss cells (Guan *et al.*, 2023). However,
454 UmV-KP4 does not induce major growth defects, necrosis, chlorosis or cell death when
455 over-expressed in transgenic wheat, corn or tobacco (Clausen *et al.*, 2000; Schlaich *et*
456 *al.*, 2006; Quijano *et al.*, 2016; Deb *et al.*, 2018). UmV-KP6α and UmV-KP6β associate
457 to form a stable heterodimer (Li *et al.*, 1999). UmV-KP6α appears necessary for
458 recognition of susceptible cells, through a mechanism involving the N-terminal α helix,
459 while UmV-KP6β is required for toxicity (Allen *et al.*, 2013b). However, the molecular
460 mechanism underpinning the toxicity of UmV-KP6α/β to fungal cells is unknown (Allen
461 *et al.*, 2013b), although it has been hypothesised that this complex forms membrane
462 pores (Li *et al.*, 1999).

463

464 **Zt-KP6-1 and Zt-KP4-1 are antifungal proteins**

465

466 Neither Zt-KP4-1 nor Zt-KP6-1 induced necrosis when infiltrated into wheat leaves.
467 Similarly, Fg-KP4L-2 from *F. graminearum* did not induce necrosis of wheat leaves (Lu
468 & Faris, 2019). Still, recombinant Fg-KP4L-2 slightly inhibited the growth of wheat roots
469 (Lu & Faris, 2019). This is reminiscent of the low activity of UmV-KP4 on *A. thaliana*
470 root growth (Allen *et al.*, 2008). We showed that both Zt-KP4-1 and Zt-KP6-1 inhibited
471 the growth of *Z. tritici* and *B. cinerea*. Within *U. maydis*, UmV-KP4 and UmV-KP6 were
472 only toxic to susceptible strains (Allen *et al.*, 2013b). However, UmV-KP4 inhibited the
473 growth of other fungi such as *Tilletia caries*, *Ustilago tritici*, *Alternaria alternata* and
474 *Phoma exigua* (Deb *et al.*, 2018), but not the yeast *S. cerevisae* (Park *et al.*, 1994).
475 When overexpressed in transgenic wheat or tobacco, UmV-KP4 conferred resistance
476 to, respectively, *T. caries* and *U. tritici* (Clausen *et al.*, 2000; Schlaich *et al.*, 2006;
477 Quijano *et al.*, 2016), and *A. alternata* and *P. exigua* (Deb *et al.*, 2018). UmV-KP6 was
478 also toxic to the yeast *Brettanomyces bruxellensis* (Santos *et al.*, 2011), but not *S.*
479 *cerevisae* (Tao *et al.*, 1990; Santos *et al.*, 2011). The structure-activity relationship of
480 Zt-KP6-1 likely differs from UmV-KP6α/β as it did not require the formation of a
481 heterodimer to be toxic (Li *et al.*, 1999; Allen *et al.*, 2013b). In addition, Zt-KP6-1 does
482 not have the N-terminal α-helical extension of UmV-KP6α critical for its toxicity (Li *et*
483 *al.*, 1999; Allen *et al.*, 2013b). Since structural homologs of Zt-KP4-1 and Zt-KP6-1 are
484 widespread in fungi, it is tempting to speculate that some of these KP4 and KP6
485 proteins are toxic to fungi. Recent work on plant pathogenic fungi highlighted effectors
486 with antimicrobial activities (Snelders *et al.*, 2022). For instance, the cotton pathogenic
487 fungus *Verticiulium dahliae* secretes several effectors during host xylem invasion that
488 have an antibacterial activity (Snelders *et al.*, 2020). These antimicrobial effectors
489 changed the composition of the xylem and root bacterial microbiota of host plants
490 (Snelders *et al.*, 2021, 2023). In particular, VdAve1, an effector with antibacterial
491 activity, specifically inhibits the growth of *Sphingomonas* bacteria, which act
492 antagonistically toward *V. dahliae* in the host plant rhizosphere (de Jonge *et al.*, 2012;
493 Snelders *et al.*, 2020). AMAPEC, a machine-learning based computational software
494 using shared structural and physicochemical properties of known antimicrobial
495 proteins, identified a large number of candidate antimicrobial proteins among effectors
496 of three different plant-associated fungi (Mesny & Thomma, 2024). This finding
497 suggests that fungi have extended repertoires of antimicrobial effectors. We have used

498 AMAPEC to predict the antimicrobial activities of the KP4 and KP6 proteins we
499 identified. Interestingly most of these KP6 and KP4 proteins, including Zt-KP4-1 and
500 Zt-KP6-1, were predicted to have antimicrobial activities by AMAPEC (83% of KP6,
501 77% of KP4, Sup Table 5).
502
503 **Fungal KP4 and KP6 proteins are wide spread in fungi and define novel**
504 **structural superfamilies**
505
506 Using a novel pipeline, we identified a large number of KP4 and KP6 structural
507 homologs in fungi. This novel pipeline is based on (i) FoldSeek structure similarity
508 searches using AF2 structural models of fungal secreted proteins, combined with (ii)
509 HMM pattern searches relying on Zt-KP4/UmV-KP4 or Zt-KP6/UmV-KP6α conserved
510 cysteine patterns and (iii) structure-based manual curation (Sup. Fig. 11; FHAT
511 (Foldseek Hmmer Alphafold TMalign) in Figure 7). The topology and structure of KP4
512 and KP6 proteins were manually compared to Zt-KP4/UmV-KP4 or Zt-KP6/UmV-
513 KP6α. This procedure discriminated proteins with a true KP4 or KP6 structural fold
514 from proteins with limited or no structural similarity. To compare our dataset (FHAT)
515 with those of two recent systematic structural studies on fungal effectors (Seong:
516 Seong & Krasileva, 2023; Derbyshire: Derbyshire & Raffaele, 2023), we clustered all
517 the KP4 and KP6 proteins identified in these three studies into families of highly related
518 proteins (at least 90% sequence identity and 60% coverage). This analysis identified
519 1737 KP4 families for FHAT, 227 for Seong and 333 for Derbyshire, as well as 559
520 KP6 families for FHAT, 97 for Seong and 80 for Derbyshire. This result was expected
521 since we have analyzed more fungal species than the two previous studies. We have
522 then compared these datasets for the seven species shared across these three studies
523 (Figure 7). For example, in *Z. tritici*, 60% of the FHAT KP4 and KP6 were jointly
524 identified by Seong and Derbyshire (Figure 7). Adding KP4 and KP6 detected only by
525 FHAT and Seong and those detected only by FHAT and Derbyshire increased the
526 number of KP4 and KP6 shared between FHAT and either Seong or Derbyshire to
527 80%. Eleven putative KP4 and two putative KP6 were specifically detected by
528 Derbyshire in *Z. tritici*. However, the manual analysis of their structures showed that
529 they do not have the KP4 or the KP6 fold. Therefore, these proteins are likely false
530 positive from this pipeline. No false positive were detected in *Z. tritici* by Seong. The
531 same trend was observed for the six other species (Figure 7). This result suggested

532 that the FHAT method is more efficient than methods used in these two previous
533 analyses (slightly more KP4 and KP6 detected, less false positive).
534
535 KP4 and KP6 proteins were found in *ascomycotina* and *basidiomycotina* with different
536 lifestyles, including plant pathogens, plant symbionts and saprophytes. A notable
537 exception were animal fungal pathogens which did not have KP4 proteins. Contrary to
538 KP6 proteins, KP4 proteins were identified in plants. Some plant KP4 clustered with
539 Fg-KP4 and UmV-KP4 (kcl02-E), as observed by Brown (2011), Lu and Faris (2019),
540 and Guan (2023). Another cluster (kcl01-R) included 175 plant KP4 proteins containing
541 the same Pfam domain (PF1657) found in some plant antifungal proteins such as
542 Ginkgobilobin-2.

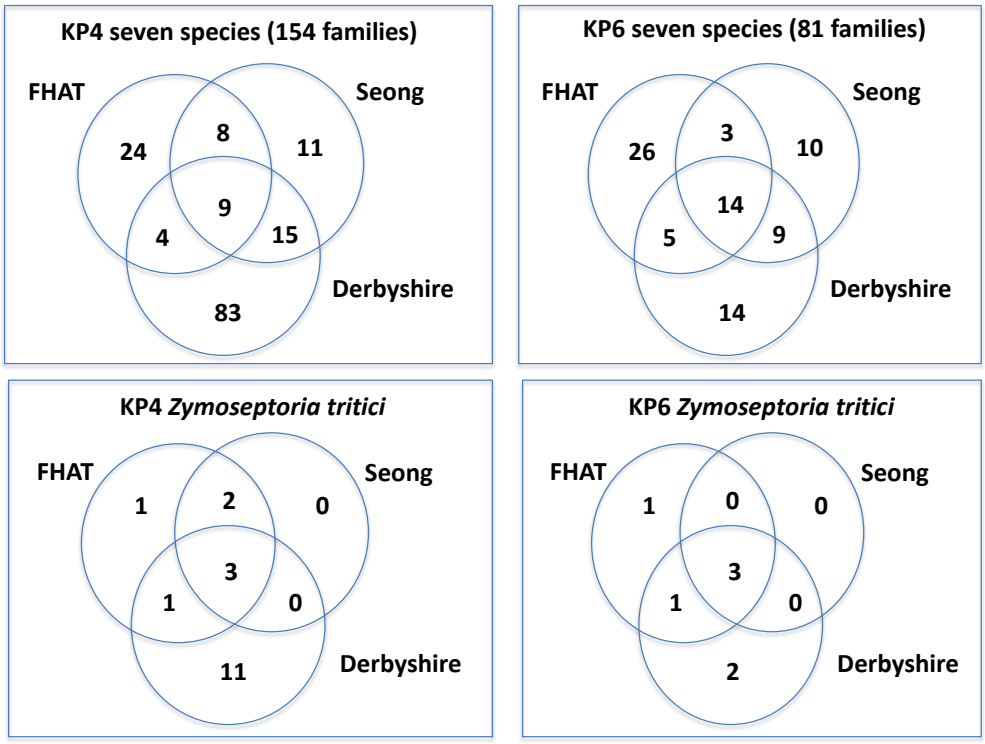

543
544
545 Figure 7. Venn Diagram comparing KP4 and KP6 proteins identified by different
546 structural classification methods.
547 Comparison between the FHAT protocol (Sup. Fig. 10) to other structural classification
548 methods (Seong:(Seong & Krasileva, 2023)), (Derbyshire:(Derbyshire & Raffaele,
549 2023)). KP4 and KP6 protein sequences identified in the seven fungal species

550 analysed by the three studies were clustered into families with at least 90% sequence
551 identity and 60% sequence overlap. The numbers of effector families detected by one
552 or more methods are indicated in the Venn diagrams for KP4 and KP6 proteins of either
553 the seven species or only Z. tritici included in the seven species analysed.
554
555 Classification of the KP4 proteins according to their structural similarities using PCA
556 and DALI Z-scores (see Fig. 6) revealed four structural super families not identified
557 before. Group-1 only contained proteins carrying the KP4 domain including Fg-KP4-1,
558 Fg-KP4-2, Fg-KP4-3, UmV-KP4, and 396 proteins from clusters kcl02-A, kcl02-E and
559 klc02-I. This group overlaps with the KP4 super family defined using Fg-KP4 and UmV-
560 KP4 by Lu and Faris (2019), and Brown (2011) that includes proteins carrying the KP4
561 Pfam domain and some plant KP4 (Guan *et al.*, 2023). Group-2 overlaps with the ECP2
562 super family that includes proteins carrying the HCE2 Pfam domain (Stergiopoulos *et*
563 *al.*, 2012). However, ECP2 proteins were not yet predicted to have a KP4 fold. This
564 structural group included *Zt*-KP4-1, Zt-KP4-2 and Zt-KP4-3, ECP2 proteins, and 402
565 proteins from the clusters kcl01-D, kcl01-Q, kcl07-A, kcl10-A and kcl14-A. Among KP4
566 proteins from structural Groups-1 and 2, only UmV-KP4 (Group-1) and Zt-KP4-1
567 (Group-2) were tested for their toxicity to fungi. It is tempting to speculate that members
568 of these two structural groups, including ECP2, are fungitoxic. This hypothesis has to
569 be investigated by testing the biological activity of a wide array of KP4 proteins.
570 Groups-3 and -4 included proteins that did not have HCE2 or KP4 domains, and mostly
571 (90%) no Pfam domain. Since none of these KP4 proteins have been studied, it will be
572 interesting to assess their biological activity.
573
574 Classification of the KP6 proteins according to their structural similarities using PCA
575 and DALI Z-scores (Fig. 5) revealed three structural super families not identified before.
576 Group-1 gathered proteins structurally related to AvrLm10A and AvrLm6 from *L.*
577 *maculans,* SIX5 from *F. oxysporum*, and 25 fungal proteins from the kcl04-C cluster,
578 but no proteins from *Zymoseptoria*. AvrLm6 and AvrLm10A were already shown to
579 have a structural fold similar to Zt-KP6-1 and UmV-KP6α (Talbi *et al.*, 2023; Loubet *et*
580 *al.*, 2024). AvrLm10A and SIX5 physically interact with effectors generally encoded by
581 neighboring genes (Ma *et al.*, 2015; Petit-Houdenot *et al.*, 2019; Yu *et al.*, 2023; Talbi
582 *et al.*, 2023), and they facilitate the symplastic transport of their partner protein in host
583 plant tissues (Ma *et al.*, 2015; Talbi *et al.*, 2023). The biological activity of Group-1 KP6

584 proteins towards fungi is unknown. Group-2 included proteins structurally related to
585 known effectors such as BAS4 from *P. oryzae* (Khang *et al.*, 2010) and *ECP28* from
586 *P. fulvum* (Mesarich *et al.*, 2018). BAS4 is expressed during the biotrophic stage of
587 rice infection by *P. oryzae*, and restricted to the biotrophic interface between the fungal
588 cell wall and the plant membrane of the infected rice cells (Khang *et al.*, 2010). This
589 structural group includes Zt-KP6-4, and 420 KP6 proteins from clusters kcl01-C, kcl02-
590 G, kcl04-A, kcl11, and UmV-KP6β. Group-3 contained proteins related to Zt-KP6-1 and
591 UmV-KP6α. It also includes Zt-KP6-2, Zt-KP6-6, and five proteins from cluster kcl02-
592 A. Since Group-2 and -3 include three proteins with antifungal activities (UmV-KP6β,
593 Zt-KP6-1, UmV-KP6α), one may predict that some proteins from these two groups will
594 be fungitoxic. This hypothesis needs to be confirmed by testing the biological activity
595 of a wide array of KP6 proteins on fungi.
596
597

598 MATERIELS AND METHODS

599

600 **Protein expression and purification**

601 The Zt-KP6 mature protein (residues 21-90) was expressed with the pET-SP vector,
602 produced and purified as previously described (de Guillen *et al.*, 2015). The Zt-KP4
603 protein was expressed with the pET derived plasmid pdbccdb-3C-His, produced and
604 purified as previously described (Lahfa *et al.*, 2024) (Supplementals File S1) .

605

606 **Nuclear magnetic resonance spectroscopy**

607 To generate isotopically labelled samples for NMR spectroscopy, we used $^{15}NH_4Cl$, as
608 the unique source of nitrogen. The samples containing 0,7 mM of purified protein in
609 10 % D_2O and 1 µM DSS as a reference were analyzed using an 800 MHz Avance
610 Bruker spectrometer and a TCI probe at 303 K. Spectra were recorded with Topspin
611 3.2 (Bruker) and referenced to DSS (4,4-dimethyl-4-silapentane-1-sulfonic acid) for the
612 ^{1}H dimension and indirectly for the ^{15}N dimension. NMR data were processed using
613 Topspin 3.6 (Bruker) and analyzed with the in-house software Cindy 2.1 (Padilla,
614 www.cbs.cnrs.fr). Side chain assignments were carried out using 2D-NOESY, 2D-
615 TOCSY and COSY-DQF experiments with D_2O samples, combined with ^{15}N-NOESY-
616 HSQC and ^{15}N-TOCSY-HSQC 3D spectra. The CYANA 3 program (Güntert, 2004)
617 was used for automatic NOE assignments and structure calculations. The CANDID
618 procedure of CYANA was used to assign the 3D-peaks list from the ^{15}N-NOESY-HSQC
619 spectra. Structures were analyzed with PROCHECK (Laskowski *et al.*, 1993).
620 Refinement statistics for the structure are listed in Sup. Table 1. The structure of Zt-
621 KP6 was deposited in the Protein Data Bank and in BMRB with accession number
622 9GWD and ID 34963 respectively.

623

624 **X-ray crystallography**

625 The purified protein Zt-KP6 was concentrated to 10 mg/ml in 20 mM Tris-HCl, pH 8.0,
626 150 mM NaCl, 1 mM DTT. The purified protein Zt-KP4 was concentrated to 8 mg/ml in
627 20 mM NaCi, pH 5.6, 150 mM NaCl, 1 mM DTT. Crystallization trials were performed
628 at 20°C by the hanging-drop vapor-diffusion method in 96-well microplates using a
629 Mosquito HTS robot with 100 nl of protein mixed with 100 nl of reservoir. After 3 weeks,
630 Zt-KP6 crystals were obtained from the condition 0.01 M $NiCl_2$, 0.1 M Tris pH 8.5, 1M
631 $LiSO_4$ (from classic kit, Hampton research®). After refinement and soaking in tantalum,

632 diffraction crystals were obtained in 0.1M Tris pH 9, 1.5M $LiSO_4$, 100mM $ZnSO_4$. After
633 2 weeks, small crystals of Zt-KP4 were obtained from one condition of the Peg kit
634 (Qiagen®) containing 0.1M sodium acetate pH 4.6 and 30%(v/v) PEG 300. All crystals
635 were flash frozen in liquid nitrogen.
636
637 **Data collection, processing and structure determination**
638 Crystal diffraction datasets were collected at the European Synchrotron Radiation
639 Facility (ESRF, Grenoble). For Zt-KP6, data were collected at beam line ID30A-1
640 (Svensson *et al.*, 2015, 2018; Bowler *et al.*, 2015, 2016; Nurizzo *et al.*, 2016) using a
641 Pixel detector (Pilatus3-2M) and processed by XDS (Kabsch, 2010) and AIMLESS
642 (Evans, 2011), from the CCP4/CCP4i programs suite (Potterton *et al.*, 2003; Winn *et*
643 *al.*, 2011). For Zt-KP4, data were collected at beam line ID30B (Mueller-Dieckmann *et*
644 *al.*, 2015; McCarthy *et al.*, 2018) using a Pixel detector (PILATUS3 6M) and auto
645 processed by XDSAPP (Krug *et al.*, 2012; Sparta *et al.*, 2016). Zt-KP6 crystals belong
646 to the $P2_12_12_1$ space group and contain two molecules in the asymmetric unit. The
647 structure of Zt-KP6 was determined to 1.36 Å by the single wavelength anomalous
648 diffraction (SAD) method using HKL2MAP (Pape & Schneider, 2004; Sheldrick, 2010).
649 Zt-KP4 crystals belong to the H3 space group and contain eight molecules in the
650 asymmetric unit. The structure of Zt-KP4 was determined by molecular replacement
651 with Molrep (Vagin & Teplyakov, 1997) from CCP4I2 (Winn *et al.*, 2011) using the
652 model determined by AF2 (Jumper *et al.*, 2021). After modelbuilding using arp/warp
653 (Langer *et al.*, 2008), Coot (Emsley *et al.*, 2010) and refinement by REFINE from
654 PHENIX (Adams *et al.*, 2010; Afonine *et al.*, 2012) final structures had R(%) / R(%)free
655 of 14 / 18.3 for Zt-KP6 and 17.5 / 21.9 for Zt-KP4. Data collection and
656 refinement statistics for the structures are listed in Sup. Table 2. Figures were
657 generated using PyMol v1.6 (http://www.pymol.org/). The atomic coordinates and
658 structure factors of Zt-KP6 and Zt-KP4, were deposited in the Protein Data Bank with
659 accession numbers 6QPK and 8ACX respectively.
660
661 **Biological assays of Zt-KP4-1 and Zt-KP6-1**
662 Zt-KP4-1 and Zt-KP6-1 were infiltrated into leaves of the wheat cultivar Taichung 29 at
663 a concentration of 2 µM. As a control, the necrotrophic effector ToxA from *P. nodorum*
664 (Tan *et al.*, 2012) was infiltrated into Taichung 29 wheat leaves at concentrations from
665 0.2 to 2 µM. *Z. tritici* IPO323 isolate and the necrotrophic plant pathogen *Botrytis*

666 *cinerea* were used for growth assays in 96 well microtiter plates containing liquid potato
667 dextrose growth medium (PDA). Each well of the plate was filled with 100µL of PDA
668 containing either 10E6 *Z. tritici* spores/mL or 10E6 *B. cinerea* spores/mL and different
669 concentrations of Zt-KP4-1 or Zt-KP6-1 (0.55, 1.65 and 5.5 µM). 96 well plates were
670 incubated in the dark at either 18°C (*Z. tritici*) or 25°C (*B. cinerea*) with shaking (50
671 rpm). After 7 days of growth, the OD at 580 nm was recorded on a spectrophotometer.
672 The % of inhibition was calculated according to the formula: % inhibition = ((OD
673 treated/OD control)-1)*100. Values displayed in Table 1 were the mean ± Standard
674 Error Deviation (SED) from three independent experiments.
675
676 **FHAT protocol for the detection of fungal KP4 and KP6 proteins**
677 Fungal KP4 and KP6 proteins were retrieved from public databases according to the
678 following protocol (Sup Figure 10) and result files for each step are available at URLs
679 https://pat.cbs.cnrs.fr/kp4/fhat_kp4 and https://pat.cbs.cnrs.fr/kp6/fhat_kp6. The
680 protocol for the detection of fungal KP4 and KP6 proteins is fully described in the
681 legend of Sup Figure 10.
682
683 **PCA analysis**
684 To classify KP4 and KP6 proteins according to their structural similarities, an ”all
685 against all” analysis was performed for both families using the DALI server (Holm,
686 2020). This computing delivered matrices of all the Z-scores for each pair of proteins.
687 If a pair of proteins had a Z-score of 0.1, they were excluded from the following step.
688 A Principal Component Analysis (PCA) was performed using these Z-scores matrices
689 using *Statistic Kingdom*
690 (https://www.statskingdom.com/410multi_linear_regression.html). Protein names
691 were directly labeled on the graphs.
692
693 **Acknowledgements**
694 The CBS is a member of the France-BioImaging (FBI) and the French Infrastructure
695 for Integrated Structural Biology (FRISBI), 2 national infrastructures supported by the
696 French National Research Agency (ANR-10-INBS-0004 and ANR-10-INBS-0005,
697 respectively). We thank R. Lambert for assistance with protein production and x-ray
698 crystallography. We are grateful to Matthew Bowler and Didier Nurizzo at the European
699 Synchrotron Radiation Facility (ESRF), Grenoble, France for providing assistance in

using beamline ID30B and ID30A-1 and the ESRF for provision of synchrotron radiation facilities via Block Allocation Group beamtime.

Data availability

The data that support the findings of this study are openly available at the following URLs:
https://pat.cbs.cnrs.fr/kp4/fhat_kp4
https://pat.cbs.cnrs.fr/kp6/fhat_kp6

Authors contributions

KDG, AP, TK and MHL planned and designed the research. KDG, LM, JG, PB, FH, ML, JR, YPH and MHL performed experiments and analysed data. KDG, AP, TK and MHL wrote the manuscript.

715 **List of figures and table:**

716

717 **Figure 1. Crystal structures of (A) Zt-KP6-1 (6QPK chain A) and (B) UmV-KP6α**
718 **(4GVB chain A).**

719 The numbering of the residues in the pdb file corresponds to the purified recombinant
720 protein (Fig sup1 A4) starting with the GHM sequence which is a remainder of the TEV
721 protease cleavage site. For the full protein, the residue numbering starts at the next
722 alanine at position 20 in the mature protein. Structures are colored in rainbow colors
723 from blue (N terminus) to red (C terminus). For Zt-KP6-1 the loop connecting β1 (in
724 blue) to α1 (in cyan) was not observed in the density and is shown by a blue dashed
725 line. Disulphide bonds are shown in grey and labelled Dx. For the D1 (C26-C86) bond
726 in Zt-KP6-1, both conformations are shown.

727

728 **Figure 2. Crystal structures of (A) Zt-KP4-1 (8ACX chain A) and (B) UmV-KP4**
729 **(1KPT chain A).**

730 Structures are colored in rainbow colors from blue (N terminus) to red (C terminus).
731 For Zt-KP4 the loops connecting β6 to β7 and β6 to α1 were not observed in the density
732 and are shown by dashed lines. Disulphide bonds are shown in grey and labelled Dx.

733

734

735 **Figure 3. Phylogenetic tree of *Zymoseptoria* KP6-1 and KP6-2**

736 MAFFT alignment, BMGE cleaning, PhyML Phylogenetic tree using NGPhylogeny.fr
737 (Lemoine *et al.*, 2019). Bootstrap values > 70% are indicated under each branch after
738 the supported node. Midpoint tree rooting. Zt-KP6-1_Ztritici_3D7: Uniprot
739 A0A1X7RM13 (identical to Zt-KP6-1_IPO323); Zt-KP6-1_Ztritici_1E4: Uniprot
740 A0A2H1G421, PDB 6QKP; Zp-KP6-1_Zpseudotritici: JGI Zymps1_802032; Zt-KP6-
741 2_Ztritici_1E4: Uniprot A0A2H1H0K4; Zt-KP6-2_Ztritici_IPO323: Uniprot F9XLY9; Zt-
742 KP6-2_Ztritici_3D7: Uniprot A0A1X7S5L2; Zb-KP6-2_Zbrevis: Uniprot A0A0F4GMG5;
743 Za-KP6-2_Zardabiliae: JGI Za_774343 ; Zp-KP6-2_Zpseudotritici: JGI
744 Zymps1_805921.

745

746 **Figure 4. Phylogenetic tree of *Zymoseptoria* KP4-1, KP4-2, and KP4-3**

747 MAFFT alignment, BMGE cleaning, PhyML Phylogenetic tree using NGPhylogeny.fr
748 (Lemoine *et al.*, 2019). Bootstrap values > 70% are indicated under each branch after

749 the supported node. Tree root with Ecp2_Passalora fulva and
750 Ecp2_Pseudocercospora fijiensis as outgroups. Zt-KP4-1_Ztritici_IPO323: re-
751 annotated NIP1/Mycgr3-106176 see Sup. Fig1; Zt-KP4-1_Ztritici_1E4: Uniprot
752 A0A2H1H404; Zt-KP4-1_Ztritici_3D7: Uniprot A0A1X7S6U3; Zt-KP4-1_Ztritici_1A5:
753 Uniprot A0A1Y6M012; Zt-KP4-2_Ztritici_IPO323: Mycgr3-107904, Uniprot F9X223;
754 Zb-KP4-2_Zbrevis: KJY02238, Uniprot A0A0F4GYX0; Zt-KP4-3_Ztritici_IPO323:
755 Mycgr3-111636, Uniprot F9XQ02; Zt-KP4-3_Ztritici_3D7: Uniprot A0A1X7S9R6; Zb-
756 KP4-3_Zbrevis: KJX96086, Uniprot A0A0F4GF74; Ecp2_Passalora fulva: Uniprot
757 Q00365; Ecp2_Pseudocercospora fijiensis: Uniprot M2Z6V3; Ecp2_Sphaerulina
758 musiva: Uniprot N1QK49; Ecp2_Cochliobolus sativus: Uniprot M2TE34
759
760 **Figure 5. Classification of fungal KP6 families according to their structures**
761 DALI all by all analysis followed by a PCA using a DALI score matrix (Holm, 2020).
762 meta-cluster kclXX, cluster AFDB50 kclXX-Y, (number of proteins in AFDB50 cluster),
763 Uniprot representative (example A0A2H1G421): kcl01-C, (100), A0A4V3HRP1,
764 M1W1H7; kcl01-L, (65), SIX5 = A0A010RIE2, AvrLm10A = E5A720_LEPMJ; kcl02-A,
765 (5), A0A4R8TM13; kcl02-D, (138), Zt-KP6-4 = A0A2H1GZA7; kcl02-G, (321),
766 A0A135SXI2; BAS4 = BAS4_MAGO7, Lm-KP6 = E5A0W1_LEPMJ; kcl04-A, (1),
767 F9FAC2; kcl04-C, (25), AvrLm6 = A0A010QJV2; AvrLm6 = E5R515_LEPMJ; kcl06-A,
768 (6), Zb-KP6-2 = A0A0F4GMG5, Zt-KP6-2 = A0A2H1H0K4; kcl06-B, (3), Zt-KP6-1 =
769 A0A2H1G421/6QKP; kcl07-A, (5), Zt-KP6-5 = A0A2H1FMK1, Zb-KP6-6 =
770 A0A0F4GGQ1; kcl11-A, (6), A0A317AKI4; kcl14-A, (93), ECP28-2 = A0A1P8YXM1,
771 ECP28-3 = A0A1P8YXM5; kcl14-B, (14), ECP28-1 = A0A1P8YXQ5; LmXXXX,
772 *Leptosphaeria* KP6 proteins, (8 protein, Loubet et al. 2024); Vi-KP6-famXX, *Venturia*
773 KP6 proteins, (4 families, Rocafort et al. 2022); White circle, UmV-KP6α, 4gvbA, White
774 circle, UmV-KP6β, 4gvbB
775
776 **Figure 6. Classification of fungal KP4 families according to their structures**
777 DALI all by all analysis followed by a PCA using a DALI score matrix (Holm, 2020).
778 meta-cluster kclXX, cluster AFDB50 kclXX-Y, (number of proteins in AFDB50 cluster),
779 Uniprot representative (example A0A2H1H404): kcl01-D, (83), Zt-KP4-1 =
780 A0A2H1H404/8ACX; kcl01-Q, (203), Sm-ECP2 = N1QK49, Psf-ECP2 = M2Z6V3, Paf-
781 ECP2 = Q00365; kcl02-A, (15), A0A4U0XEI9; kcl02-E, (256), Fg-KP4-2 =
782 A0A3S7E9S6, Fg-KP4-3 = A0A2H3GQS6; kcl02-I, (125), Fg-KP4-1 = A0A2H3GK41;

783 klc02-0, (324), Zt-KP4-9 = A0A2H1GXX1; kcl05-A, (14), A0A6A6DAE0; kcl07-A, (53),
784 A0A177DVW3; kcl07-C, (35), Zt-KP4-2 = A0A2H1FWY7; Zt-KP4-3 = A0A1Y6M296;
785 kcl08-A, (5), S3D5P; kcl09-A, (14), M3BT27; kcl09-B, (131), Zt-KP4-6 =
786 A0A2H1GNH3, Zt-KP4-7 = A0A2H1GND9; kcl10-A, (16), A0A1L9SH47; kcl12-A, (9),
787 E3L0Y8; kcl14-C, (12), A0A0A1V5R3; kcl18-A, (9), Zt-KP4-5 = A0A2H1GP20; kcl21-
788 A, (13), A0A0J9W663; kcl27-A, (39), A0A4T0WCM2; kcl38-A, (8), A0A017SS08;
789 White circle, UmV-KP4 = kptA.
790
791 **Figure 7. Venn Diagram comparing KP4 and KP6 fungal proteins identified by**
792 **different pipelines**
793 KP4 and KP6 fungal proteins identified by recent systematic structural studies on
794 fungal effectors (Seong & Krasileva, 2023; Derbyshire & Raffaele, 2023) were
795 compared to our dataset (FHAT). Zt-KP6-1 to 5 and Zt-KP4-1 to 5 were not detected
796 by Krasileva (2023) and Raffaele (2023).
797
798 **Table1. Toxicity of Zt-KP4-1 and Zt-KP6-1 to fungi**
799 The percentage of growth inhibition of *B. cinerea* and *Z. tritici* were plotted for 3
800 different concentrations of ToxA from *Phaeosphaeria nodorum*, Zt-KP4-1 and Zt-KP6-
801 1. Values are the mean ± standard deviation from three experiments.
802
803

804 **List of supplementary figures and tables:**

805

806 **Supplementary Figure 1. Annotation of IPO323 *Z. tritici* Zt-Mycgr3-91409 (Zt-KP6-**
807 **1) and Zt-Mycgr3-106176 (Zt-KP4-1)**

808 Sup. Fig.1-A Annotation of IPO323 *Z. tritici* CDS Zt-Mycgr3-91409 (Zt-KP6-1)

809 Sup. Fig.1-B Annotation of IPO323 *Z. tritici* CDS Zt-Mycgr3-106176 (Zt-KP4-1)

810

811 **Supplementary Figure 2 Purification of Zt-KP6-1 by gel filtration**

812 Gel filtration profile and SDS-PAGE analysis of purified Zt-KP6-1. Sizes of the
813 molecular mass markers are indicated on the left of the gel.

814

815 **Supplementary Figure 3 NMR analysis of Zt-KP6-1**

816 HSQC spectra of Zt-KP6-1 at, 0.7 mM in 20 mM NaCitrate pH 5.4, 150 mM NaCl, 1
817 mM DTT, 303 K, 800 MHz. Cross-peak assignments are indicated using one-letter
818 amino acid and number (the asterisk shows a folded red peak). Missing residue N36.

819

820 **Supplementary Figure 4 Topology diagrams of Zt-KP6-1 and UmV-KP6α**

821 The structures were processed by PDBsum and the secondary structures were colored
822 from N-terminus (blue) to C-terminus (red) according to Figure 1. Disulfide Bonds (D)
823 are represented as gray lines.

824

825 **Supplementary Figure 5 Purification of Zt-KP4-1 by gel filtration**

826 Gel filtration profile and SDS-PAGE analysis of purified Zt-KP4-1. (a) dimer, (b)
827 monomer. Sizes of the molecular mass markers are indicated on the left of the gel.

828

829 **Supplementary Figure 6 Dimer of Zt-KP4-1 between chains B (cyan) and G (blue)**

830 Residues involved in hydrogen bonds at the dimer interface are labelled and
831 represented by sticks. Hydrophobics residues involved in the pocket are highlighted in
832 lines and coloured in yellow. According to the GenBank sequence SMR60557.1, the
833 residue numbering must start after the signal peptide at residue S20. T33 in the
834 structure corresponds to T48 in the GenBank sequence.

835

836 **Supplementary Figure 7 Topology diagrams of Zt-KP4 and UmV-Kp4**

837 The structures were processed by PDBsum and the secondary structure were colored
838 from N-terminus (blue) to C-terminus (red) according to the Figure 2. Disulfide Bonds
839 (D) are represented as gray lines.
840
841 **Supplementary Figure 8 Structure and topology of Zt-KP6-1 and Zt-KP6-2**
842 Zt-KP6-2 structure was predicted by AlphaFold-2. The structures were processed by
843 PDBsum and the secondary structure were coloured from N-terminus (blue) to C-
844 terminus (red) according to Figure 1.
845
846 **Supplementary Figure 9 Structure and topology of Zt-KP4-1, Zt-KP4-2 and Zt-**
847 **KP4-3**
848 Zt-KP4-1, Zt-KP4-2 and Zt-KP4-3 structures were predicted by AlphaFold-2. The
849 structures were processed by PDBsum and the secondary structure were coloured
850 from N-terminus (blue) to C-terminus (red) according to the Figure 2.
851
852 **Supplementary Figure 10 Flow chart of the pipeline used to identify fungal**
853 **proteins structurally related to Zt-KP6-1 and Zt-KP4-1**
854
855 **Supplementary Figure 11 Expression of Zt-KP4-1, Zt-KP4-2, Zt-KP4-3, Zt-KP6-1,**
856 **Zt-KP6-2, Zt-KP6-4 and Zt-KP6-6 during infection of wheat leaves infection.**
857 RNAseq data from Rudd et al. (2015). RPKM (fungal RNAseq Reads Per Kilobase
858 Million)
859
860 **Supplementary Table 1. NMR and refinement statistics for Zt-KP6-1**
861 (Zt-KP6-1, 0.7 mM, 20 mM NaCitrate pH 5.4, 150 mM NaCl, 1 mM DTT, 303 K, 800
862 MHz) PDB:9GWD BMRB ID 34963
863
864 **Supplementary Table 2. X-ray data collection and refinement statistics for Zt-**
865 **KP6-1 and Zt-KP4-1**
866 #Rmerge = Shkl Si |Ii(hkl) - (I(hkl))| / Shkl Si Ii(hkl), where *Ii(hkl)* is the *i*th observation
867 of reflection *hkl* and <*I(hkl)*> is the weighted average intensity for all observations of
868 reflection *hkl*.
869

870 **Supplementary Table 3 List of the proteins structurally related to Zt-KP6-1**
871 **detected using our pipeline**
872
873 **Supplementary Table 4 List of the proteins structurally related to Zt-KP4-1**
874 **detected using our pipeline**
875
876 **Supplementary Table 5 Prediction of the antimicrobial activity of fungal KP4 and**
877 **KP6 proteins using AMAPEC (Mesny & Thomma, 2024)**
878
879 **Supplementary file S1 Nucleotide sequence of synthetic genes and plasmids**
880 **used in this study**
881

References

Adams PD, Afonine PV, Bunkóczi G, Chen VB, Davis IW, Echols N, Headd JJ, Hung L-W, Kapral GJ, Grosse-Kunstleve RW, *et al.* 2010. *PHENIX* : a comprehensive Python-based system for macromolecular structure solution. *Acta Crystallographica Section D Biological Crystallography* **66**: 213–221.

Afonine PV, Grosse-Kunstleve RW, Echols N, Headd JJ, Moriarty NW, Mustyakimov M, Terwilliger TC, Urzhumtsev A, Zwart PH, Adams PD. **2012**. Towards automated crystallographic structure refinement with *phenix.refine*. *Acta Crystallographica Section D Biological Crystallography* **68**: 352–367.

Allen A, Chatt E, Smith TJ. **2013a**. The Atomic Structure of the Virally Encoded Antifungal Protein, KP6. *Journal of Molecular Biology* **425**: 609–621.

Allen A, Islamovic E, Kaur J, Gold S, Shah D, Smith TJ. **2013b**. The virally encoded killer proteins from Ustilago maydis. *Fungal Biology Reviews* **26**: 166–173.

Allen A, Snyder AK, Preuss M, Nielsen EE, Shah DM, Smith TJ. **2008**. Plant defensins and virally encoded fungal toxin KP4 inhibit plant root growth. *Planta* **227**: 331–339.

Badet T, Oggenfuss U, Abraham L, McDonald BA, Croll D. **2020**. A 19-isolate reference-quality global pangenome for the fungal wheat pathogen Zymoseptoria tritici. *BMC biology* **18**: 12.

Battache M, Lebrun M-H, Sakai K, Soudière O, Cambon F, Langin T, Saintenac C. **2022**. Blocked at the Stomatal Gate, a Key Step of Wheat Stb16q-Mediated Resistance to Zymoseptoria tritici. *Frontiers in Plant Science* **13**.

Bauer S, Yu D, Lawson AW, Saur IML, Frantzeskakis L, Kracher B, Logemann E, Chai J, Maekawa T, Schulze-Lefert P. **2021**. The leucine-rich repeats in allelic barley MLA immune receptors define specificity towards sequence-unrelated powdery mildew avirulence effectors with a predicted common RNase-like fold (B Kobe, Ed.). *PLOS Pathogens* **17**: e1009223.

Ben M'Barek S, Cordewener JHG, Tabib Ghaffary SM, van der Lee TAJ, Liu Z, Mirzadi Gohari A, Mehrabi R, America AHP, Robert O, Friesen TL, *et al.* 2015. FPLC and liquid-chromatography mass spectrometry identify candidate necrosis-inducing proteins from culture filtrates of the fungal wheat pathogen Zymoseptoria tritici. *Fungal Genetics and Biology* **79**: 54–62.

Blondeau K, Blaise F, Graille M, Kale SD, Linglin J, Ollivier B, Labarde A, Lazar N, Daverdin G, Balesdent M, *et al.* 2015. Crystal structure of the effector A vr L m4–7 of *Leptosphaeria maculans* reveals insights into its translocation into plant cells and recognition by resistance proteins. *The Plant Journal* **83**: 610–624.

Bowler MW, Nurizzo D, Barrett R, Beteva A, Bodin M, Caserotto H, Delagenière S, Dobias F, Flot D, Giraud T, *et al.* 2015. MASSIF-1: a beamline dedicated to the fully automatic characterization and data collection from crystals of biological macromolecules. *Journal of Synchrotron Radiation* **22**: 1540–1547.

Bowler MW, Svensson O, Nurizzo D. **2016**. Fully automatic macromolecular crystallography: the impact of MASSIF-1 on the optimum acquisition and quality of data. *Crystallography Reviews* **22**: 233–249.

Brown DW. **2011**. The KP4 killer protein gene family. *Current Genetics* **57**: 51–62.

Cao Y, Kümmel F, Logemann E, Gebauer JM, Lawson AW, Yu D, Uthoff M, Keller B, Jirschitzka J, Baumann U, *et al.* 2023. Structural polymorphisms within a common powdery mildew effector scaffold as a driver of coevolution with cereal immune receptors. *Proceedings of the National Academy of Sciences of the United States of America* **120**: e2307604120.

Carreón-Anguiano KG, Gómez-Tah R, Pech-Balan E, Ek-Hernández GE, De los Santos-Briones C, Islas-Flores I, Canto-Canché B. **2023**. Pseudocercospora fijiensis Conidial

Germination Is Dominated by Pathogenicity Factors and Effectors. *Journal of Fungi* **9**.
Chang T-C, Salvucci A, Crous PW, Stergiopoulos I. **2016**. Comparative Genomics of the Sigatoka Disease Complex on Banana Suggests a Link between Parallel Evolutionary Changes in Pseudocercospora fijiensis and Pseudocercospora eumusae and Increased Virulence on the Banana Host. *PLoS genetics* **12**: e1005904.
Clausen M, Kräuter R, Schachermayr G, Potrykus I, Sautter C. **2000**. Antifungal activity of a virally encoded gene in transgenic wheat. *Nature biotechnology* **18**: 446–449.
Deb D, Shrestha A, Maiti IB, Dey N. **2018**. Recombinant Promoter (MUASCsV8CP) Driven Totiviral Killer Protein 4 (KP4) Imparts Resistance Against Fungal Pathogens in Transgenic Tobacco. *Frontiers in Plant Science* **9**: 278.
Derbyshire MC, Raffaele S. **2023**. *Surface frustration re-patterning underlies the structural landscape and evolvability of fungal orphan candidate effectors*. Genomics.
Ebert MK, Rangel LI, Spanner RE, Taliadoros D, Wang X, Friesen TL, de Jonge R, Neubauer JD, Secor GA, Thomma BPHJ, *et al.* 2021. Identification and characterization of Cercospora beticola necrosis-inducing effector CbNip1. *Molecular Plant Pathology* **22**: 301–316.
Emsley P, Lohkamp B, Scott WG, Cowtan K. **2010**. Features and development of *Coot*. *Acta Crystallographica Section D Biological Crystallography* **66**: 486–501.
Evans PR. **2011**. An introduction to data reduction: space-group determination, scaling and intensity statistics. *Acta Crystallographica Section D Biological Crystallography* **67**: 282–292.
Finkler A, Peery T, Tao J, Bruenn J, Koltin igal. **1992**. Immunity and resistance to the KP6 toxin of Ustilago maydis. *Molecular and General Genetics MGG* **233**: 395–403.
Gage MJ, Bruenn J, Fischer M, Sanders D, Smith TJ. **2001**. KP4 fungal toxin inhibits growth in Ustilago maydis by blocking calcium uptake: KP4 fungal toxin mechanism. *Molecular Microbiology* **41**: 775–785.
Gage MJ, Rane SG, Hockerman GH, Smith TJ. **2002**. The Virally Encoded Fungal Toxin KP4 Specifically Blocks L-Type Voltage-Gated Calcium Channels. *Molecular Pharmacology* **61**: 936–944.
Gu F, Khimani A, Rane SG, Flurkey WH, Bozarth RF, Smith TJ. **1995**. Structure and function of a virally encoded fungal toxin from Ustilago maydis: a fungal and mammalian Ca2+ channel inhibitor. *Structure* **3**: 805–814.
Guan Y, Ma L, Wang Q, Zhao J, Wang S, Wu J, Liu Y, Sun H, Huang J. **2023**. Horizontally acquired fungal killer protein genes affect cell development in mosses. *The Plant Journal* **113**: 665–676.
de Guillen K, Ortiz-Vallejo D, Gracy J, Fournier E, Kroj T, Padilla A. **2015**. Structure Analysis Uncovers a Highly Diverse but Structurally Conserved Effector Family in Phytopathogenic Fungi. *PLOS Pathog* **11**: e1005228.
Güntert P. **2004**. Automated NMR structure calculation with CYANA. *Methods in molecular biology (Clifton, N.J.)* **278**: 353–378.
Holm L. **2020**. DALI and the persistence of protein shape. *Protein Science* **29**: 128–140.
de Jonge R, van Esse HP, Maruthachalam K, Bolton MD, Santhanam P, Saber MK, Zhang Z, Usami T, Lievens B, Subbarao KV, *et al.* 2012. Tomato immune receptor Ve1 recognizes effector of multiple fungal pathogens uncovered by genome and RNA sequencing. *Proceedings of the National Academy of Sciences of the United States of America* **109**: 5110–5115.
Jumper J, Evans R, Pritzel A, Green T, Figurnov M, Ronneberger O, Tunyasuvunakool K, Bates R, Žídek A, Potapenko A, *et al.* 2021. Highly accurate protein structure prediction with AlphaFold. *Nature* **596**: 583–589.
Kabsch W. **2010**. Integration, scaling, space-group assignment and post-refinement. *Acta*

Crystallographica Section D Biological Crystallography **66**: 133–144.
Kettles GJ, Bayon C, Sparks CA, Canning G, Kanyuka K, Rudd JJ. **2018**. Characterization of an antimicrobial and phytotoxic ribonuclease secreted by the fungal wheat pathogen Zymoseptoria tritici. *New Phytologist* **217**: 320–331.
Khang CH, Berruyer R, Giraldo MC, Kankanala P, Park S-Y, Czymmek K, Kang S, Valent B. **2010**. Translocation of Magnaporthe oryzae Effectors into Rice Cells and Their Subsequent Cell-to-Cell Movement. *The Plant Cell* **22**: 1388–1403.
Kilaru S, Fantozzi E, Cannon S, Schuster M, Chaloner TM, Guiu-Aragones C, Gurr SJ, Steinberg G. **2022**. Zymoseptoria tritici white-collar complex integrates light, temperature and plant cues to initiate dimorphism and pathogenesis. *Nature Communications* **13**: 5625.
Koltin Y. **1988**. The killer system of Ustilago maydis: secreted polypeptides encoded by viruses. *Viruses of fungi and simple eukaryotes*: 209–242.
Krug M, Weiss MS, Heinemann U, Mueller U. **2012**. *XDSAPP* : a graphical user interface for the convenient processing of diffraction data using *XDS*. *Journal of Applied Crystallography* **45**: 568–572.
Lahfa M, Barthe P, De Guillen K, Cesari S, Raji M, Kroj T, Le Naour—Vernet M, Hoh F, Gladieux P, Roumestand C, *et al.* 2024. The structural landscape and diversity of Pyricularia oryzae MAX effectors revisited (F Mesny, Ed.). *PLOS Pathogens* **20**: e1012176.
Langer G, Cohen SX, Lamzin VS, Perrakis A. **2008**. Automated macromolecular model building for X-ray crystallography using ARP/wARP version 7. *Nature Protocols* **3**: 1171–1179.
Lapalu N, Simon A, Demenou B, Paumier D, Guillot M-P, Gout L, Suffert F, Valade R. **2023**. Complete Genome Sequences of Septoria linicola: A Resource for Studying a Damaging Flax Pathogen. *Molecular plant-microbe interactions : MPMI* **36**: 59–63.
Laskowski RA, MacArthur MW, Moss DS, Thornton JM. **1993**. PROCHECK: a program to check the stereochemical quality of protein structures. *Journal of Applied Crystallography* **26**: 283–291.
Lazar N, Mesarich CH, Petit-Houdenot Y, Talbi N, Li De La Sierra-Gallay I, Zélie E, Blondeau K, Gracy J, Ollivier B, Blaise F, *et al.* 2022. A new family of structurally conserved fungal effectors displays epistatic interactions with plant resistance proteins (B Kobe, Ed.). *PLOS Pathogens* **18**: e1010664.
Lazar N, Mesarich CH, Petit-Houdenot Y, Talbi N, de la Sierra-Gallay IL, Zélie E, Blondeau K, Gracy J, Ollivier B, Blaise F, *et al.* 2020. *A new family of structurally conserved fungal effectors displays epistatic interactions with plant resistance proteins*. Plant Biology.
Le Naour—Vernet M, Charriat F, Gracy J, Cros-Arteil S, Ravel S, Veillet F, Meusnier I, Padilla A, Kroj T, Cesari S, *et al.* 2023. Adaptive evolution in virulence effectors of the rice blast fungus Pyricularia oryzae (MF Seidl, Ed.). *PLOS Pathogens* **19**: e1011294.
Lemoine F, Correia D, Lefort V, Doppelt-Azeroual O, Mareuil F, Cohen-Boulakia S, Gascuel O. **2019**. NGPhylogeny.fr: new generation phylogenetic services for non-specialists. *Nucleic acids research* **47**: W260–W265.
Li N, Erman M, Pangborn W, Duax WL, Park C-M, Bruenn J, Ghosh D. **1999**. Structure of Ustilago maydis Killer Toxin KP6 α-Subunit. *Journal of Biological Chemistry* **274**: 20425–20431.
Li G, Newman M, Yu H, Rashidzade M, Martínez-Soto D, Caicedo A, Allen KS, Ma L-J. **2024**. Fungal effectors: past, present, and future. *Current Opinion in Microbiology* **81**: 102526.
Lima AM, Azevedo MIG, Sousa LM, Oliveira NS, Andrade CR, Freitas CDT, Souza PFN. **2022**. Plant antimicrobial peptides: An overview about classification, toxicity and clinical applications. *International journal of biological macromolecules* **214**: 10–21.

Lo Presti L, Lanver D, Schweizer G, Tanaka S, Liang L, Tollot M, Zuccaro A, Reissmann S, Kahmann R. **2015**. Fungal Effectors and Plant Susceptibility. *Annual Review of Plant Biology* **66**: 513–545.
Loubet C, Li de la Sierra-Gallay I, van Tilbeurgh H, Fudal I. **2024**. Decoding plant pathogen strategies: exploring Leptosphaeria maculans effector structural insights for enhanced plant resistance. *Submitted*.
Lu S, Faris JD. **2019**. Fusarium graminearum KP4-like proteins possess root growth-inhibiting activity against wheat and potentially contribute to fungal virulence in seedling rot. *Fungal Genetics and Biology* **123**: 1–13.
Ma L, Houterman PM, Gawehns F, Cao L, Sillo F, Richter H, Clavijo-Ortiz MJ, Schmidt SM, Boeren S, Vervoort J, *et al.* 2015. The AVR2–SIX5 gene pair is required to activate I-2-mediated immunity in tomato. *New Phytologist* **208**: 507–518.
McCarthy AA, Barrett R, Beteva A, Caserotto H, Dobias F, Felisaz F, Giraud T, Guijarro M, Janocha R, Khadrouche A, *et al.* 2018. ID30B – a versatile beamline for macromolecular crystallography experiments at the ESRF. *Journal of Synchrotron Radiation* **25**: 1249–1260.
Mesarich CH, Ökmen B, Rovenich H, Griffiths SA, Wang C, Karimi Jashni M, Mihajlovski A, Collemare J, Hunziker L, Deng CH, *et al.* 2018. Specific Hypersensitive Response–Associated Recognition of New Apoplastic Effectors from *Cladosporium fulvum* in Wild Tomato. *Molecular Plant-Microbe Interactions* **31**: 145–162.
Mesny F, Thomma BP. **2024**. *AMAPEC: accurate antimicrobial activity prediction for fungal effector proteins*. Microbiology.
Mueller-Dieckmann C, Bowler MW, Carpentier P, Flot D, McCarthy AA, Nanao MH, Nurizzo D, Pernot P, Popov A, Round A, *et al.* 2015. The status of the macromolecular crystallography beamlines at the European Synchrotron Radiation Facility. *The European Physical Journal Plus* **130**: 70.
Nurizzo D, Bowler MW, Caserotto H, Dobias F, Giraud T, Surr J, Guichard N, Papp G, Guijarro M, Mueller-Dieckmann C, *et al.* 2016. RoboDiff: combining a sample changer and goniometer for highly automated macromolecular crystallography experiments. *Acta Crystallographica Section D Structural Biology* **72**: 966–975.
Outram MA, Figueroa M, Sperschneider J, Williams SJ, Dodds PN. **2022**. Seeing is believing: Exploiting advances in structural biology to understand and engineer plant immunity. *Current Opinion in Plant Biology*: 8.
Pape T, Schneider TR. **2004**. ıt HKL2MAP: a graphical user interface for macromolecular phasing with ıt SHELX programs. *Journal of Applied Crystallography* **37**: 843–844.
Park C-M, Bruenn JA, Ganesa C, Flurkey WF, Bozarth RF, Koltin Y. **1994**. Structure and heterologous expression of the Ustilago maydis viral toxin KP4. *Molecular Microbiology* **11**: 155–164.
Pennington HG, Jones R, Kwon S, Bonciani G, Thieron H, Chandler T, Luong P, Morgan SN, Przydacz M, Bozkurt T, *et al.* 2019. The fungal ribonuclease-like effector protein CSEP0064/BEC1054 represses plant immunity and interferes with degradation of host ribosomal RNA. *PLOS Pathogens* **15**: e1007620.
Petit-Houdenot Y, Degrave A, Meyer M, Blaise F, Ollivier B, Marais C-L, Jauneau A, Audran C, Rivas S, Veneault-Fourrey C, *et al.* 2019. A two genes – for – one gene interaction between Leptosphaeria maculans and Brassica napus. *New Phytologist* **223**: 397–411.
Potterton E, Briggs P, Turkenburg M, Dodson E. **2003**. A graphical user interface to the CCP4 program suite. *Acta crystallographica. Section D, Biological crystallography* **59**: 1131–1137.
Quijano CD, Wichmann F, Schlaich T, Fammartino A, Huckauf J, Schmidt K, Unger C,

Broer I, Sautter C. 2016. KP4 to control Ustilago tritici in wheat: Enhanced greenhouse resistance to loose smut and changes in transcript abundance of pathogen related genes in infected KP4 plants. *Biotechnology Reports* **11**: 90–98.

Rocafort M, Bowen JK, Hassing B, Cox MP, McGreal B, de la Rosa S, Plummer KM, Bradshaw RE, Mesarich CH. 2022. The Venturia inaequalis effector repertoire is dominated by expanded families with predicted structural similarity, but unrelated sequence, to avirulence proteins from other plant-pathogenic fungi. *BMC Biology* **20**: 246.

Rudd JJ, Kanyuka K, Hassani-Pak K, Derbyshire M, Andongabo A, Devonshire J, Lysenko A, Saqi M, Desai NM, Powers SJ, *et al.* 2015. Transcriptome and metabolite profiling of the infection cycle of Zymoseptoria tritici on wheat reveals a biphasic interaction with plant immunity involving differential pathogen chromosomal contributions and a variation on the hemibiotrophic lifestyle definition. *Plant physiology* **167**: 1158–1185.

Santos A, Navascués E, Bravo E, Marquina D. 2011. Ustilago maydis killer toxin as a new tool for the biocontrol of the wine spoilage yeast Brettanomyces bruxellensis. *International journal of food microbiology* **145**: 147–154.

Schlaich T, Urbaniak BM, Malgras N, Ehler E, Birrer C, Meier L, Sautter C. 2006. Increased field resistance to Tilletia caries provided by a specific antifungal virus gene in genetically engineered wheat. *Plant biotechnology journal* **4**: 63–75.

Seong K, Krasileva KV. 2023. Prediction of effector protein structures from fungal phytopathogens enables evolutionary analyses. *Nature Microbiology* **8**: 174–187.

Sheldrick GM. 2010. Experimental phasing with *SHELXC / D / E* : combining chain tracing with density modification. *Acta Crystallographica Section D Biological Crystallography* **66**: 479–485.

Snelders NC, Boshoven JC, Song Y, Schmitz N, Fiorin GL, Rovenich H, van den Berg GCM, Torres DE, Petti GC, Prockl Z, *et al.* 2023. A highly polymorphic effector protein promotes fungal virulence through suppression of plant-associated Actinobacteria. *The New phytologist* **237**: 944–958.

Snelders NC, Petti GC, van den Berg GCM, Seidl MF, Thomma BPHJ. 2021. An ancient antimicrobial protein co-opted by a fungal plant pathogen for in planta mycobiome manipulation. *Proceedings of the National Academy of Sciences of the United States of America* **118**.

Snelders NC, Rovenich H, Petti GC, Rocafort M, van den Berg GCM, Vorholt JA, Mesters JR, Seidl MF, Nijland R, Thomma BPHJ. 2020. Microbiome manipulation by a soil-borne fungal plant pathogen using effector proteins. *Nature plants* **6**: 1365–1374.

Snelders NC, Rovenich H, Thomma BPHJ. 2022. Microbiota manipulation through the secretion of effector proteins is fundamental to the wealth of lifestyles in the fungal kingdom. *FEMS microbiology reviews* **46**.

Spanu PD. 2017. Cereal immunity against powdery mildews targets RNase-Like Proteins associated with Haustoria (RALPH) effectors evolved from a common ancestral gene. *New Phytologist* **213**: 969–971.

Sparta KM, Krug M, Heinemann U, Mueller U, Weiss MS. 2016. *XDSAPP2.0*. *Journal of Applied Crystallography* **49**: 1085–1092.

Stergiopoulos I, Kourmpetis YAI, Slot JC, Bakker FT, De Wit PJGM, Rokas A. 2012. In Silico Characterization and Molecular Evolutionary Analysis of a Novel Superfamily of Fungal Effector Proteins. *Molecular Biology and Evolution* **29**: 3371–3384.

Svensson O, Gilski M, Nurizzo D, Bowler MW. 2018. Multi-position data collection and dynamic beam sizing: recent improvements to the automatic data-collection algorithms on MASSIF-1. *Acta Crystallographica Section D Structural Biology* **74**: 433–440.

Svensson O, Malbet-Monaco S, Popov A, Nurizzo D, Bowler MW. 2015. Fully automatic characterization and data collection from crystals of biological macromolecules. *Acta*

Crystallographica Section D Biological Crystallography **71**: 1757–1767.
Talbi N, Fokkens L, Audran C, Petit-Houdenot Y, Pouzet C, Blaise F, Gay EJ, Rouxel T, Balesdent M, Rep M, *et al.* 2023. The neighbouring genes *AvrLm10A* and *AvrLm10B* are part of a large multigene family of cooperating effector genes conserved in Dothideomycetes and Sordariomycetes. *Molecular Plant Pathology* **24**: 914–931.
Tan K-C, Ferguson-Hunt M, Rybak K, Waters ODC, Stanley WA, Bond CS, Stukenbrock EH, Friesen TL, Faris JD, McDonald BA, *et al.* 2012. Quantitative Variation in Effector Activity of ToxA Isoforms from Stagonospora nodorum and Pyrenophora tritici-repentis. *Molecular Plant-Microbe Interactions®* **25**: 515–522.
Tao J, Ginsberg I, Banerjee N, Held W, Koltin Y, BRUENNl JA. **1990**. Ustilago maydis KP6 Killer Toxin: Structure, Expression in Saccharomyces cerevisiae, and Relationship to Other Cellular Toxins. *MOL. CELL. BIOL.* **10**: 9.
Teulet A, Quan C, Evangelisti E, Wanke A, Yang W, Schornack S. **2023**. A pathogen effector FOLD diversified in symbiotic fungi. *New Phytologist*: nph.18996.
Vagin A, Teplyakov A. **1997**. *MOLREP* : an Automated Program for Molecular Replacement. *Journal of Applied Crystallography* **30**: 1022–1025.
Van den Ackerveken GF, Van Kan JA, Joosten MH, Muisers JM, Verbakel HM, De Wit PJ. **1993**. Characterization of two putative pathogenicity genes of the fungal tomato pathogen Cladosporium fulvum. *Molecular plant-microbe interactions : MPMI* **6**: 210–215.
Winn MD, Ballard CC, Cowtan KD, Dodson EJ, Emsley P, Evans PR, Keegan RM, Krissinel EB, Leslie AGW, McCoy A, *et al.* 2011. Overview of the *CCP* 4 suite and current developments. *Acta Crystallographica Section D Biological Crystallography* **67**: 235–242.
Yu DS, Outram MA, Smith A, McCombe CL, Khambalkar PB, Rima SA, Sun X, Ma L, Ericsson DJ, Jones DA, *et al.* 2023. *The structural repertoire of Fusarium oxysporum f. sp. lycopersici effectors revealed by experimental and computational studies*. elife.
Zhang Y, Skolnick J. **2005**. TM-align: a protein structure alignment algorithm based on the TM-score. *Nucleic acids research* **33**: 2302–2309.